

Long-Term Fuel-Optimal Collision Avoidance Maneuvers with Station-Keeping Constraints

Zeno Pavanello*, Laura Pirovano[†] and Roberto Armellin[‡]
The University of Auckland, Auckland, 1010, New Zealand

This work presents a sequential convex program method to compute fuel-optimal collision avoidance maneuvers for long-term encounters. The low-thrust acceleration model is used to account for the control, but the method can compute high-thrust maneuvers by increasing the maximum available acceleration. Dealing with the long-term conjunction poses additional challenges compared to the short-term problem because the encounter is not instantaneous. Thus, under the assumption of Gaussian statistics, the probability of collision is replaced by a simpler metric, the instantaneous probability of collision (IPoC) and a keep-out zone constraint is formulated as a continuous condition to be respected throughout the time frame of interest. The robustness of the solution is improved by introducing a constraint on the sensitivity of the IPoC. Furthermore, the collision avoidance problem is coupled with the classical station-keeping requirement for geostationary Earth orbit satellites and with a return to the nominal orbit condition for low Earth orbit satellites. Even though no guarantee is given for the recovery of the global optimum solution, numerical simulations in different orbital regimes show that the proposed approach can yield a local fuel-optimal solution with a run-time suitable for autonomous applications.

I. Introduction

The space population is rapidly increasing. As of the end of 2022, more than 32,000 objects larger than 10 cm are being tracked in space, and the active space population has doubled in the last four years [1]. The increase in the number of operational spacecraft is mainly due to miniaturization (e.g., CubeSats) and the launch of mega-constellations (e.g., Starlink). In parallel, the number of tracked space debris is growing thanks to improved monitoring systems (e.g., the space fence system). This situation brings new challenges in space situational awareness and spacecraft operations.

One of these is the risk of collision between space objects. The probability of a conjunction event occurring increases

*PhD candidate, Te Pūnaha Ātea - Space Institute, 20 Symonds Street, Auckland Central, Auckland 1010, New Zealand; zpav176@aucklanduni.ac.nz (Corresponding Author).

[†]Research Fellow, Te Pūnaha Ātea - Space Institute, 20 Symonds Street, Auckland Central, Auckland 1010, New Zealand; laura.pirovano@auckland.ac.nz.

[‡]Professor, Te Pūnaha Ātea - Space Institute, 20 Symonds Street, Auckland Central, Auckland 1010, New Zealand; roberto.armellin@auckland.ac.nz. Member AIAA.

A part of this work was presented at the 33rd AAS/AIAA Space Flight Mechanics Meeting, held in Austin, Texas, January 15-19 2023. Paper 23-104 was entitled "Long-Term Encounters Collision Avoidance Maneuver Optimization with a Convex Formulation".

with the increasing density of the orbital regime [2], as indicated by research conducted in both low Earth orbit (LEO) [3] and geostationary Earth orbit (GEO) [4]. In recent times, there has been a significant increase in research focusing on collision avoidance (CA). In particular, the development of autonomous and fuel-optimized collision avoidance maneuvers (CAMs) aims to effectively decrease operational expenses, minimize reliance on human intervention, and extend the lifespan of missions by mitigating propellant wastage. Conjunction events are typically considered too risky when the probability of collision (PoC) is greater than an arbitrary threshold. NASA identifies two such thresholds, corresponding respectively to the yellow and the red warning: the former is 10^{-5} , and the latter is 10^{-4} [5]. When these limits are exceeded, a CAM is designed to lower the value of probability of collision (PoC) while respecting operational constraints, if required.

Conjunctions can be divided into two major types: short-term and long-term. The former is the most common and has been investigated more thoroughly. In this circumstance, the relative velocity involved is high, and the collision is almost instantaneous: the conjunction dynamics can be approximated as linear without loss of accuracy, and the event is studied on the two-dimensional B-plane [6–8]. In long-term conjunctions, the two objects move on similar orbits, and the event cannot be considered instantaneous [9]. Patera [10] shows that when the relative trajectory of the primary spacecraft with respect to the secondary is far from a straight line inside the combined covariance ellipsoid, the encounter can be classified as long-term and a different model must be used. Despite many recent attempts at finding ways to efficiently compute PoC for long-term encounters [11–15], non-rectilinear relative trajectories inside the uncertainty ellipsoid render the risk quantification and, consequently, the design of long-term CAMs very complex. In a recent publication [9], Núñez Garzón and Lightsey have suggested that instantaneous probability of collision (IPoC) is a valuable proxy for PoC: in general, an increase in PoC is accompanied by a high value of IPoC, so controlling the evolution of IPoC allows to indirectly control the growth of PoC. For this reason, in agreement with a good portion of the state-of-the-art [9, 16–19], we use IPoC as a risk metric rather than the more complex PoC.

CA strategies have been developed for long-term encounters in terms of linear program (LP) [20] and deterministic disjunctive LP [21]. In reference [20], Mueller simplifies the relative motion using a linear time-varying system and converts the CA problem into an LP. To this end, the ellipsoidal keep-out-zone (KOZ) constraint is linearized into a hemisphere. Moreover, to keep the problem linear, the l^1 norm of the control is minimized, which can result in higher propellant consumption if compared with the l^2 norm. Notably, Mueller’s approach does not take the uncertainty of the states into account; instead, the KOZ region is arbitrarily defined by the author. In this work, we will demonstrate that the evolution of the uncertainty is a key aspect of the definition of the KOZ in the long-term encounter, which was first addressed by Serra *et al.* [21]. They formulate a deterministic disjunctive LP. They linearize the dynamics using the Yamanaka-Ankersen state transition matrix (STM), which is also used to propagate the covariance in a linear fashion. In this approach, since a relative motion model is used, the combined covariance is propagated from the time of closest approach (TCA) to the desired final time. This may lead to inaccuracies because the difference between the orbits of the

two spacecraft, which results in different STMs, is not considered. Like in our approach, PoC is substituted by IPoC, but this variable is not directly controlled. Instead, a polyhedral KOZ constraint is employed, and IPoC is only checked a posteriori in the validation process. Furthermore, the same l^1 norm of the control is used, as in Mueller’s approach.

This paper investigates a convex formulation of the problem to mitigate current limitations. Under the hypothesis that the Gaussian states are known at TCA (from a conjunction data message), we assume that the uncertainties evolve linearly and independently from the control action. With respect to the previously cited approaches, linear propagation of the covariance is carried out separately for the two spacecraft, using the STMs of an accurate dynamics model that includes all the relevant orbital perturbations.

The use of convex optimization to solve trajectory design problems is particularly appealing as it has been proven to be efficient for many aerospace applications [22], from short-term CAMs [7, 23] to asteroid landing [24], drone formation flying [25], or spacecraft maneuver estimation [26]. These contributions have shown that it is convenient to use a second-order cone program (SOCP) to formulate the convexified problem because this enables the minimization of the l^2 norm of the control history, which is a fundamental requirement in spacecraft trajectory optimization problems. To frame the problem into a SOCP, all of the non-convex parts of the original optimal control problem (OCP) must be convexified [27], most notably the fuel-optimal objective function, the nonlinear dynamics constraint, and the PoC constraint. In the proposed method, additional control magnitude variables and a lossless relaxation are introduced to make the objective function linear and transform the constraint on control magnitude into a second-order cone. The nonlinear dynamics are automatically linearized using differential algebra (DA), and the associated STMs are used to propagate the covariances of the spacecraft.

The convexification approach for the PoC constraint proposed in reference [7] for short-term encounters is extended to long-term encounters. In reference [7], the author transcribes the PoC constraint using the squared Mahalanobis distance (SMD), effectively turning it into a KOZ condition on the B-plane; this KOZ is convexified by means of a projection and linearization algorithm. We propose an analogous approach where we define a three-dimensional SMD based on IPoC, and we iteratively approximate the KOZ constraint into a succession of hemispaces. Unlike in the short-term encounter case, the SMD constraint is applied to the whole window of interest and not only at the nominal conjunction time. To guarantee a robust solution, a novel constraint is introduced to limit the sensitivity of IPoC to state uncertainties. As a result, safety is ensured even in the presence of thrust misalignment or guidance, navigation, and control errors. The initial stochastic problem is therefore reduced into a deterministic one. This approach bears some similarity to works on robust trajectory optimization (for example, see [28], [29], and [30, 31]), in which chance constraints are converted into a deterministic form suitable for convex optimization. However, unlike these works, in the CA scenario, it is not advantageous to include a feedback component to control the covariance of the primary since most of the uncertainty is generally associated with the uncontrolled secondary. On the other hand, the state of the primary is well-known, and its uncertainty does not have sufficient time to grow significantly.

Post-CAM station keeping (SK) constraints are introduced both for GEO and for LEO scenarios. In the first case, recalling the work from Mueller *et al.* [32], a linearised keep-in-box constraint bounds the spacecraft to respect a latitude-longitude requirement; in LEO a constraint on the final state forces the spacecraft to return to its nominal orbit.

A trust region constraint based on references [33–35] to limit the solution space and favor the convergence of the algorithm is adopted. The linearization of the dynamics and IPoC constraints prevents the optimizer from finding the optimal solution with a single SOCP run. For this reason, a sequential convex program (SCP) is built as a succession of SOCPs, where the solution from the previous SOCP is taken as the linearization point for the new problem. This process can take a discretely large number of iterations before converging to the optimal solution of the original OCP. This iterative approach allows for updating the evolution of the covariance history, which might lead to changes in the shape of the KOZ that can be accounted for in the next iteration. This aspect has been neglected in the literature but might have relevance for cases in which the IPoC is highly sensitive to variation in the covariance.

The article is organized into five sections. In Section II, the dynamics of the problem are presented; in Section III, the base CAM optimization problem is posed as a SCP, and the sensitivity constraint on the collision metric is introduced. The SK constraints are introduced in Section IV, leading to the final formulation of the convex problem in Section V. The algorithm is then applied to realistic LEO, GEO and highly elliptic orbit (HEO) test cases and conclusions are drawn in Sections VI and VII respectively.

II. Formulation of the Long-Term Collision Avoidance Problem

Let the states of two spacecraft (primary and secondary) be described at time t_0 by two uncorrelated Gaussian multivariate random variables. The states are represented using any arbitrary set of elements, e.g. Cartesian, Keplerian or generalized equinoctial elements.

$$\mathbf{x}_p(t_0) \sim \mathcal{N}(\boldsymbol{\zeta}_p(t_0), \mathbf{C}_p(t_0)) \text{ and } \mathbf{x}_s(t_0) \sim \mathcal{N}(\boldsymbol{\zeta}_s(t_0), \mathbf{C}_s(t_0)), \quad (1)$$

where $\mathbf{x}_p(t_0), \mathbf{x}_s(t_0) \in \mathbb{R}^6$ are the two uncorrelated random variables, $\boldsymbol{\zeta}_p(t_0), \boldsymbol{\zeta}_s(t_0) \in \mathbb{R}^6$ are their mean values and $\mathbf{C}_p(t_0), \mathbf{C}_s(t_0) \in \mathbb{R}^{6 \times 6}$ are their covariance matrices. The control acceleration acting on the primary satellite is $\mathbf{u}(t) \in \mathbb{R}^3$. The state of the two objects can be numerically propagated using an arbitrary dynamics model, generally described as

$$\dot{\mathbf{x}}_p(t) = \mathbf{f}_p(t, \mathbf{x}_p(t), \mathbf{u}(t), \mathbf{p}_p) \text{ and } \dot{\mathbf{x}}_s(t) = \mathbf{f}_s(t, \mathbf{x}_s(t), \mathbf{p}_s), \quad (2)$$

where $t \in \mathbb{R}_{[t_0, t_f]}$ is the continuous time domain, $\mathbf{p}_p \in \mathbb{R}^{m_p}$ and $\mathbf{p}_s \in \mathbb{R}^{m_s}$ are sets of parameters, $\mathbf{f}_p(\cdot) : \mathbb{R}_{[t_0, t_f]} \times \mathbb{R}^6 \times \mathbb{R}^3 \times \mathbb{R}^{m_p} \rightarrow \mathbb{R}^6$ and $\mathbf{f}_s(\cdot) : \mathbb{R}_{[t_0, t_f]} \times \mathbb{R}^6 \times \mathbb{R}^{m_s} \rightarrow \mathbb{R}^6$ are continuous functions. In Section VI, the Accurate Integrator for Debris Analysis (AIDA) dynamics model is used, which was originally introduced in reference

[36] and implements the following acceleration vector

$$\mathbf{a}_{AIDA} = \mathbf{a}_E + \mathbf{a}_S + \mathbf{a}_M + \mathbf{a}_{drag} + \mathbf{a}_{SRP}, \quad (3)$$

where

\mathbf{a}_E is the Earth's gravitational pull computed with a potential model of order up to 15;

\mathbf{a}_S and \mathbf{a}_M are the third body accelerations of the Sun and Moon computed with NASA's Spice toolkit*;

\mathbf{a}_{drag} is the drag acceleration computed with the NRLMSISE-00 atmospheric density model and assuming a cannonball geometry for the spacecraft;

\mathbf{a}_{SRP} is the solar radiation pressure (SRP) computed with dual-cone shadow model and assuming a cannonball geometry for the spacecraft.

As proven by Baù *et al.* [37], the use of modified equinoctial elements in the propagation can preserve the Gaussian nature of the states for a much longer period compared to classical orbital elements or Cartesian coordinates. Nonetheless, when the propagation window is sufficiently short, and the state uncertainty is small, Cartesian elements can still preserve the normality of the distributions [38]. Since we are only considering propagations over one or two orbital periods, the results in Section VI are obtained using Cartesian coordinates. Nonetheless, the method is applicable to any representation of the states. To define the PoC constraint, the relative position of the primary with respect to the secondary must be made explicit. The position of the primary in Earth Centered Inertial (ECI) is a function of the state (and the same is true for the secondary):

$$\mathbf{r}_p(t) = \mathbf{h}(t, \mathbf{x}_p(t)), \quad (4)$$

where $\mathbf{h}(\cdot) : \mathbb{R} \times \mathbb{R}^6 \rightarrow \mathbb{R}^3$ is a transformation that is assumed to be quasi-linear for the uncertainty at hand. This assumption holds when the Gaussian covariances are sufficiently small. In Cartesian coordinates, this transformation simply extracts the three position coordinates of the state, as is the case in Section VI. It follows that $\mathbf{r}_p(t) \sim \mathcal{N}(\boldsymbol{\mu}_p(t), \mathbf{P}_p(t))$ and $\mathbf{r}_s(t) \sim \mathcal{N}(\boldsymbol{\mu}_s(t), \mathbf{P}_s(t))$. The relative position is then simply the subtraction of the two normally distributed random variables $\mathbf{r}_{rel}(t) = \mathbf{r}_p(t) - \mathbf{r}_s(t)$. Given that the subtraction is a linear transformation, also the relative position is normally distributed

*<https://naif.jpl.nasa.gov/naif/documentation.html>

$$\mathbf{r}_{rel}(t) \sim \mathcal{N}(\boldsymbol{\mu}(t), \mathbf{P}(t)), \quad (5a)$$

$$\boldsymbol{\mu}(t) = \boldsymbol{\mu}_p(t) - \boldsymbol{\mu}_s(t), \quad (5b)$$

$$\mathbf{P}(t) = \mathbf{P}_p(t) + \mathbf{P}_s(t). \quad (5c)$$

A. Collision Avoidance Optimal Control Problem

The original CA OCP in the continuous domain is stated as follows

$$\min_{\mathbf{u}} J = \int_{t_0}^{t_f} u(t) dt \quad (6a)$$

$$\text{s.t. } \dot{\mathbf{x}} = \mathbf{f}(\mathbf{x}(t), \mathbf{u}(t), t) \quad (6b)$$

$$P_C(t) \leq \bar{P}_C \quad (6c)$$

$$\mathbf{x}(t_0) = \mathbf{x}_0 \quad (6d)$$

$$u(t) = \sqrt{u_1(t)^2 + u_2(t)^2 + u_3(t)^2} \quad (6e)$$

$$u(t) \leq u_{max} \quad (6f)$$

where $\mathbf{u}(t) = [u_1(t) \ u_2(t) \ u_3(t)]^T$ and the state of the primary is indicated with \mathbf{x} ; $P_C(\cdot) : \mathbb{R} \rightarrow \mathbb{R}$ is the PoC function which is equal to P_C^0 at the starting time and is monotonically increasing during the conjunction; it must always be kept below the threshold \bar{P}_C . In Problem (6), Eq. (6a) is the fuel minimization objective function, Eq. (6b) is the dynamics constraint, Eq. (6c) is the PoC constraint, Eq. (6d) is the initial state bound, Eq. (6e) is a non-convex equality constraint on the control variable and Eq. (6f) is the bound on the maximum value of the control action. The mass loss due to the maneuver is not considered in the equations of motion because it is deemed negligible [7].

B. Discretization of the Dynamics

The first step towards the SOCP formulation is the discretization of Problem (6). The continuous time variable $t \in \mathbb{R}_{[t_0, t_f]}$ is substituted by the discrete time variable $t_i \in \{t_0, t_1, \dots, t_N\}$, where $N + 1$ is the number of equally spaced nodes of the discretization. Following Eq. (2) and via the use of an integration scheme - e.g., Runge-Kutta 7-8 - one

obtains the states of the two spacecraft at node $i + 1$, which depend on the state and the control at node i :

$$\mathbf{x}_{p,i+1} = \mathbf{f}_{p,i}(t_i, \mathbf{x}_{p,i}, \mathbf{u}_i, \mathbf{p}_p) \quad i \in \{0, \dots, N - 1\}, \quad (7a)$$

$$\mathbf{x}_{s,i+1} = \mathbf{f}_{s,i}(t_i, \mathbf{x}_{s,i}, \mathbf{p}_s) \quad i \in \{0, \dots, N - 1\}, \quad (7b)$$

where $\mathbf{f}_{p,i}(\cdot) : \mathbb{R}_{[t_0, t_f]} \times \mathbb{R}^6 \times \mathbb{R}^3 \times \mathbb{R}^{m_p} \rightarrow \mathbb{R}^6$ and $\mathbf{f}_{s,i}(\cdot) : \mathbb{R}_{[t_0, t_f]} \times \mathbb{R}^6 \times \mathbb{R}^{m_s} \rightarrow \mathbb{R}^6$ are the functions that describe the dynamics at node i , $\mathbf{x}_{p,i} = \mathbf{x}_p(t_i)$, $\mathbf{x}_{s,i} = \mathbf{x}_s(t_i)$ and $\mathbf{u}_i = \mathbf{u}(t_i)$. Between two consecutive nodes i and $i + 1$ the acceleration is considered constant and equal to \mathbf{u}_i . DA is used to introduce perturbations on the primary state ($\mathbf{x}_{p,i} + \delta\mathbf{x}_{p,i}$) and acceleration ($\mathbf{u}_i + \delta\mathbf{u}_i$) at each node, effectively expressing Eq. (7a) through Taylor polynomials:

$$\mathbf{x}_{p,i+1} = \mathcal{T}_{\mathbf{x}_{p,i+1}}^q(\mathbf{x}_{p,i}, \mathbf{u}_i) \quad i \in \{0, \dots, N - 1\}, \quad (8)$$

where in general the expression $\mathcal{T}_y^q(x)$ indicates the q^{th} -order Taylor expansion of the variable y as a function of x , around the expansion point \tilde{x} in which the polynomial is computed. The reader can find a detailed explanation of the use of DA in [39].

C. Selection of the Risk Metric

Probability-based criteria are the most widely employed indicators to assess the likelihood of a collision [40]. Nonetheless, many operators adopt a separation distance strategy that only relies on the objects' mean state, so no information about the uncertainty is used. In this work, the use of three distinct metrics is analyzed, namely the IPoC, which will be indicated with P_{IC} , the maximum IPoC, indicated with $P_{IC,m}$, and the separation distance d_{sep} .

The most common metric used to formulate the CA condition in the short-term CA optimization problem is PoC. Typically an upper limit is set on this variable so that at TCA $P_C < \bar{P}_C$. When considering the long-term problem, the integral formula for the computation of PoC must consider the uncertainty in the position and velocity of the two

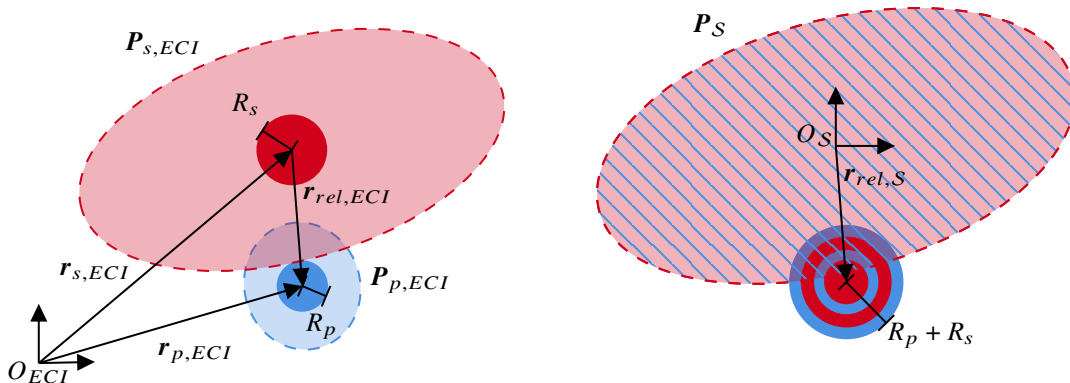


Figure 1 Left: KOZ problem in ECI frame. Right: KOZ problem in S frame.

space objects [11]. Moreover, this metric is highly nonlinear, thus unsuitable for a convex formulation. An alternative approach is setting a limit on IPoC rather than on PoC. IPoC has no dependence on the velocity uncertainty, making it simpler to compute. Additionally, IPoC can be further simplified to the SMD, indicated with d_m^2 , transforming the PoC constraint into an ellipsoidal keep-out zone, as shown in the following.

The relative position of the primary with respect to the secondary is the subtraction of the two multivariate distributions, as in Eq. (5). We define the SMD at time t as:

$$d_m^2(\mathbf{r}_{rel}(t)) = \boldsymbol{\mu}(t)^T \mathbf{P}(t)^{-1} \boldsymbol{\mu}(t). \quad (9)$$

With reference to Fig. 1, we now consider a reference frame \mathcal{S} with axes aligned to ECI and centered in the secondary spacecraft to simplify the calculations. The two spacecraft are assumed to have a spherical geometry, which is described by the hard body radius (HBR), indicated with R_p (for the primary) and R_s (for the secondary). The combined HBR of the two spacecraft is defined as the sum of their individual HBRs, $R = R_p + R_s$, and the volume of the two objects is condensed around the primary [7]. Also, we assign the whole uncertainty to the secondary spacecraft. So, $\mathbf{r}_{rel}(t)$ is shifted by an amount equal to its mean, yielding a multivariate random variable centered at the position of the secondary, defined as the origin

$$\mathbf{s}(t) = \mathbf{r}_{rel}(t) - \boldsymbol{\mu}(t) \sim \mathcal{N}(\mathbf{0}_3, \mathbf{P}(t)), \quad (10)$$

Note that in the new reference system, the primary position at time t is deterministic and equal to $\boldsymbol{\mu}(t)$: it will be indicated by the symbol $\mathbf{r}(t)$ in the following. The SMD in Eq. (9), then, becomes a measure of the distance of $\mathbf{r}(t)$ from the normal distribution $\mathbf{s}(t)$

$$d_m^2 = \mathbf{r}^T \mathbf{P}^{-1} \mathbf{r}, \quad (11)$$

where the argument t has been dropped for simplicity. The value of IPoC at the time instant t is the integral of the probability density function (PDF) over the sphere \mathbb{S}_{HBR} centered in \mathbf{r} and of radius R [21]:

$$P_{IC} = \frac{1}{(2\pi)^{3/2} \det(\mathbf{P})^{1/2}} \iiint_{\mathbb{S}_{\text{HBR}}} e^{-\mathbf{s}^T \mathbf{P}^{-1} \mathbf{s} / 2} dV, \quad (12)$$

Analogously to Alfriend and Akella's method for PoC [40], Eq. (12) can be simplified by neglecting the variation of the PDF inside the integration region. Indeed, in typical applications, the ellipsoid associated with the covariance is significantly larger than the hard body sphere [10]. The PDF, then, is evaluated only in the central point of \mathbb{S}_{HBR} ($\mathbf{s} = \mathbf{r}$), obtaining

$$P_{IC} = \sqrt{\frac{2}{\pi \det(\mathbf{P})}} \frac{R^3}{3} e^{-d_m^2/2}. \quad (13)$$

The covariance of the position might be estimated with a large margin of error; thus we might want a more conservative approach to the estimation of the collision risk. The maximum instantaneous probability of collision $P_{IC,m}$ is computed following the same procedure that is found in [40]

$$P_{IC,m} = \frac{(\sqrt{2}R)^3}{3e^1 d_m^2 \sqrt{\pi \det(\mathbf{P})}}. \quad (14)$$

From Eq. (13) or Eq. (14), it is possible to approximate a constraint on P_{IC} or on $P_{IC,m}$ into a constraint on SMD, which describes an ellipsoidal keep-out zone. Given a limit value of IPoC (\bar{P}_{IC}) or $P_{IC,m}$ ($\bar{P}_{IC,m}$), the corresponding limit of SMD alternatively becomes

$$\bar{d}_m^2 = -2 \ln\left(\frac{3\bar{P}_{IC}}{R^3} \sqrt{\frac{\pi \det(\mathbf{P})}{2}}\right), \quad (15a)$$

$$\bar{d}_m^2 = \frac{(\sqrt{2}R)^3}{3e\bar{P}_{IC,m} \sqrt{\pi \det(\mathbf{P})}}, \quad (15b)$$

and the SMD constraint at any time is stated as

$$d_m^2 \geq \bar{d}_m^2. \quad (16)$$

Alternatively to the SMD constraint, a separation distance constraint can be employed using the same formalism. Indeed, the separation distance does not provide information on the uncertainty, so it can be computed as the Mahalanobis distance of the mean state of the relative position with unit covariance $d_{sep} = \sqrt{\mathbf{r}^T \mathbf{r}}$. In this case, Eq. (16) can still be used to impose a keep-out zone condition, where the limit value is given by an arbitrarily defined distance from the secondary.

The use of IPoC as a replacement for PoC has been proposed in the literature by [9, 21]. To confirm that this is a reasonable substitution, in Fig. 2, two examples of the relationship between IPoC and PoC in relevant test cases from reference [41] are shown. Clearly, the evolution of IPoC follows the increase in PoC: when the slope of PoC is high, IPoC is non-negligible. For this reason, we can assume that controlling IPoC can be considered a reasonable alternative to reducing PoC in the long-term encounter CAM optimization problem.

1. Validity of the IPoC approximation

The validity of the IPoC approximation in Eq. (13) is determined by the entity of the variation of the PDF inside the combined hard body sphere. If the PDF changes significantly, the approximation will yield inaccurate results. An important role in this is played by the combined HBR: the smaller this value is, the less the PDF changes inside it. We analyze two cases in which the approximation behaves differently. The first case is taken from reference [9], and the second one from [41]. In the first case, the maximum variation of the PDF inside the hard body sphere is around 2×10^{-11} for an unrealistic HBR of 320 m, 1×10^{-12} for 32 m, 1.4×10^{-13} for 3.2 m, and 10^{-12} for 0.32 m. In the

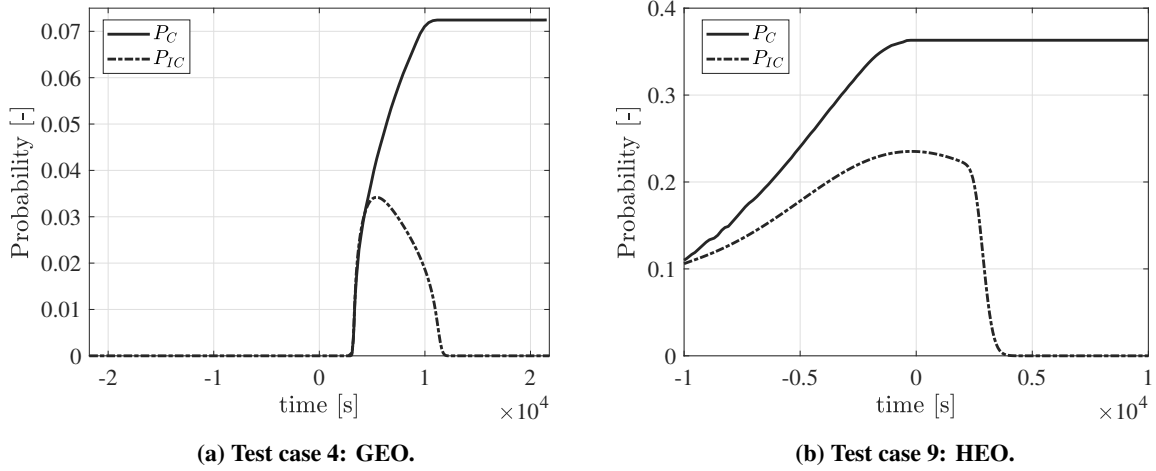


Figure 2 Comparison of IPoC and PoC for two test cases from reference [41].

second case, instead, the variations are between 0.004 and 0.04 for an HBR of 0.6 m and 12 m.

In Fig. 3, a comparison is provided between the real (Monte Carlo based) IPoC and the approximated one for the different values of HBR in the two cases. When the models are in accordance with the Monte Carlo result, the corresponding line is not visible. In Fig. 3a, we see that for HBR up to 32 m, the approximation is very accurate, and the curve starts to separate from the real IPoC only when HBR is exceedingly high. In the second scenario, represented in Fig. 3b, the approximation has a maximum relative error of 50% in the best case, where the HBR is 0.6 m, and it goes over 270.4% for the nominal case with HBR equal to 6 m. Since in typical applications, the size of the HBR is in the order of magnitude of 1 – 10 m, the approximation cannot be considered accurate for demanding scenarios like this one.

In such situations, we propose to employ a different approximation, which was introduced by Zhang *et al.* [19]. This method, referred to as "cuboid," transforms the originally spherical integration region into a parallelogram and decouples the integration into three independent one-dimensional integrals. As it can be seen from the figure, in the first scenario, this approximation can accurately follow the evolution of the real IPoC. In the second one, it is better than the constant approximation, reaching maximum errors of 3.9%, 9.5%, 20.1%, 19.6%, and 13% over the considered time span.

For this reason, we propose an inversion algorithm to obtain a SMD limit based on the cuboid IPoC to replace Eq. (15a) when the constant PDF approximation is not accurate. The algorithm is a simple non-linear program (NLP): for a generic node i , the NLP starts from point $\mathbf{r} = \mathbf{r}_i$, used to initialize the solution, to find the optimized point $\hat{\mathbf{r}} \in \mathbb{R}^3$

$$\min_{\hat{\mathbf{r}}} \quad \|\hat{\mathbf{r}} - \mathbf{r}\|, \quad (17a)$$

$$\text{s.t.} \quad P_{IC}(\mathbf{r}) = f_{cub}(\mathbf{P}, \hat{\mathbf{r}}, R) = \bar{P}_{IC}, \quad (17b)$$

$$\mathbf{r} - \Delta \mathbf{r}_{max} \leq \hat{\mathbf{r}} \leq \mathbf{r} + \Delta \mathbf{r}_{max}, \quad (17c)$$

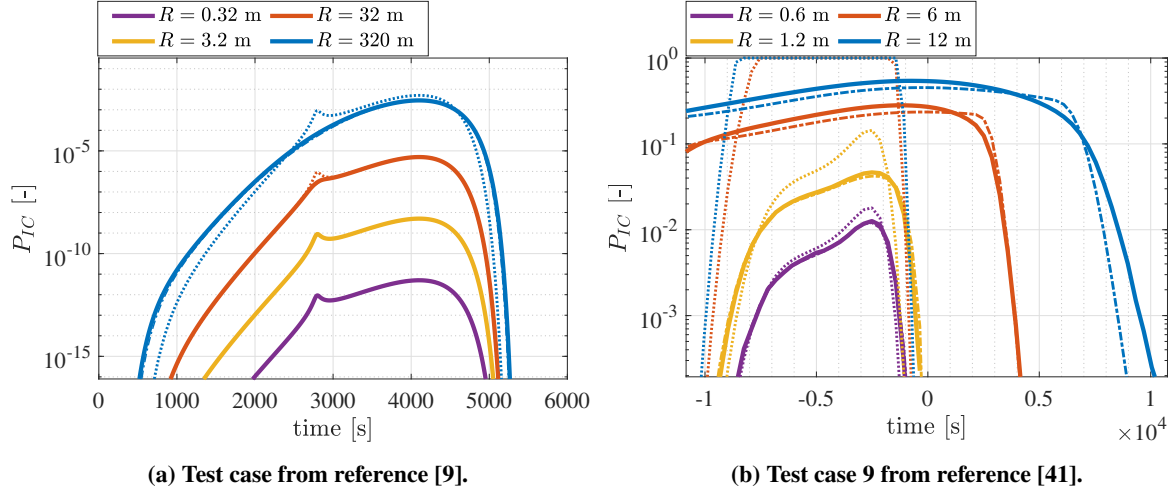


Figure 3 IPoC comparison between Monte Carlo (solid), constant (dotted), and cuboid (dash-dotted) approximations.

where $\Delta \mathbf{r} \in \mathbb{R}^3$ is a vector used to create the boundaries, and $f_{cub} : \mathbb{R}^3 \times \mathbb{R}^{3 \times 3} \times \mathbb{R}_{[0,1]} \rightarrow \mathbb{R}$ is the cuboid IPoC function. Eq. (17a) is the objective function that minimizes the distance between the optimization variable $\hat{\mathbf{r}}$ and the relative position \mathbf{r} ; Eq. (17b) imposes that the cuboid IPoC must be equal to the limit value; Eq. (17c) imposes upper and lower boundaries to the optimization variable. Once a solution has been found, the corresponding SMD threshold is computed using Eq. (9), $\bar{d}_m^2 = \hat{\mathbf{r}}^T \mathbf{P}^{-1} \hat{\mathbf{r}}$. This inversion of the IPoC limit only works in the proximity of the original point, so it performs well when the CA maneuver is small, as is the case considered in Fig. 3b, according to reference [21]. As there is no guarantee that the cuboid IPoC is constant over the surface of the ellipsoid defined by \bar{d}_m^2 , a check must be included to verify *a posteriori* that the value of IPoC computed with the cuboid approximation fulfils the required constraint. In the opposite case, a new iteration of the SCP is carried on until the constraint is met.

III. Successive Convex Program Formulation

Maneuvers can be performed at N discretization nodes in the form of a constant acceleration within the segment, \mathbf{u}_i . The last node is an exception since the acceleration would not affect the solution.

The optimization variables are the states and controls at each node. Here the covariance matrix at each node is independent of the control because there is no feedback. Hence, the scalar optimization variables are 9 for each node: the 6 components of the state and the 3 components of the control. In the following, for clarity in the formulas, the state of the primary spacecraft, that was defined in Eq. (1) as \mathbf{x}_p , will be indicated with \mathbf{x} . The full history of state and controls are expressed with the symbols $\mathbf{x} \in \mathbb{R}^{6(N+1)}$ and $\mathbf{u} \in \mathbb{R}^{3N}$

$$\mathbf{x} = \begin{bmatrix} \mathbf{x}_0^T & \mathbf{x}_1^T & \dots & \mathbf{x}_N^T \end{bmatrix}^T \quad \text{and} \quad \mathbf{u} = \begin{bmatrix} \mathbf{u}_0^T & \mathbf{u}_1^T & \dots & \mathbf{u}_{N-1}^T \end{bmatrix}^T. \quad (18)$$

Three nonlinearity sources are present in the problem: (i) the dynamics in Eq. (8) can include polynomials up to any order; (ii) the constraint in Eq. (16) is a KOZ constraint, which is a non-convex one; (iii) the minimization of the fuel expenditure requires the use of a non-convex constraint in Eq. (6e), which must be relaxed into a convex one to build the SOCP. Three main steps are then required to formulate the CAM design as a SOCP [7]. Firstly, in Section III.A the dynamics are automatically linearized using DA, and an iterative SCP method is employed. Afterward, in Section III.C the objective function and the constraint on the control acceleration magnitude are reformulated by introducing an equivalent transformation. Lastly, in Section III.D a projection and linearization approach is used to linearize the KOZ constraint. It would be more complicated to handle a constraint on IPoC since the expression is not a polynomial function of the position, and it would need a more coarse linearization than the one on SMD.

A. Linearization of the Dynamics

In general, orbital dynamics are highly non-linear and cannot be directly modeled into a convex optimization framework. To address this issue, the nonlinearities are managed through successive linearizations of the dynamics equations. The original OCP is linearized, locally, into a convex sub-problem in the framework of a SCP. This process may require numerous iterations, referred to as *major iterations* denoted by index j . Once the optimization problem of a major iteration $j - 1$ is solved, the solution $(\mathbf{x}^{j-1}, \mathbf{u}^{j-1})$ becomes available, a column vector comprising the state and control at each node. Employing DA, this solution serves as an expansion point for constructing linear dynamics maps for iteration j . The continuity condition is enforced by requiring that the state after the propagation of node i is equal to the state before the propagation of node $i + 1$. To favor the convergence of the iterations, it is advisable to normalize the control over its maximum value so that $\mathbf{u}_i \rightarrow \mathbf{u}_i / u_{max}$ and $0 \leq \|\mathbf{u}_i\| \leq 1$. In the following, the dynamics equations need to account for the normalized control, i.e., when computing the linear maps, the control must be scaled back into its original dimensions. The state and acceleration of each node are expanded around the reference points, which are the output of the previous major iteration $\tilde{\mathbf{x}}_i^j = \mathbf{x}_i^{j-1}$ and $\tilde{\mathbf{u}}_i^j = \mathbf{u}_i^{j-1}$

$$\mathbf{x}_i^j = \tilde{\mathbf{x}}_i^j + \delta \mathbf{x}_i^j \quad i \in \{0, \dots, N - 1\}, \quad (19a)$$

$$\mathbf{u}_i^j = \tilde{\mathbf{u}}_i^j + \delta \mathbf{u}_i^j \quad i \in \{0, \dots, N - 1\}, \quad (19b)$$

The state at the subsequent node is obtained through the propagation of the first-order dynamics, as in Eq. (8)

$$\mathbf{x}_{i+1}^j = \mathcal{T}_{\mathbf{x}_{i+1}^j}^1(\mathbf{x}_i^j, \mathbf{u}_i^j) \quad i \in \{0, \dots, N - 1\}. \quad (20)$$

Eq. (20) can be written in matrix form, using the linear maps that establish the first-order dynamics relationship between the perturbations before the propagation of node i and the ones after the propagation, at node $i + 1$. These maps are

$\mathbf{A}_{i+1}^j \in \mathbb{R}^{6 \times 6}$, which is the STM, and $\mathbf{B}_{i+1}^j \in \mathbb{R}^{6 \times 3}$, which is the control-state transition matrix

$$\mathbf{x}_{i+1}^j = \bar{\mathbf{x}}_{i+1}^j + \mathbf{A}_{i+1}^j \delta \mathbf{x}_i^j + \mathbf{B}_{i+1}^j \delta \mathbf{u}_i^j \quad i \in \{0, \dots, N-1\}, \quad (21)$$

where $\bar{\mathbf{x}}_{i+1} = f_{p,i}(t_i, \tilde{\mathbf{x}}_i, \tilde{\mathbf{u}}_i, \mathbf{p}_p)$ is the constant part of the DA propagation. Recalling Eq. (19), the continuity constraint can be written:

$$\mathbf{x}_{i+1}^j = \mathbf{A}_{i+1}^j \mathbf{x}_i^j + \mathbf{B}_{i+1}^j \mathbf{u}_i^j + \mathbf{c}_i^j \quad i \in \{0, \dots, N-1\}, \quad (22)$$

where \mathbf{c}_i^j is the residual of the linearization $\mathbf{c}_i^j = \bar{\mathbf{x}}_{i+1} - \mathbf{A}_{i+1}^j \tilde{\mathbf{x}}_i^j - \mathbf{B}_{i+1}^j \tilde{\mathbf{u}}_i^j$. The initial condition is fixed because the maneuver cannot alter it

$$\mathbf{x}_0^j = \mathbf{x}_0^0. \quad (23)$$

B. Propagation of the Uncertainty

It is fundamental to propagate the covariance matrices of the two spacecraft throughout the trajectory so that $\mathbf{C}_{p,i}^j$ and $\mathbf{C}_{s,i}$ are associated with each node. We assume that the uncertainty of the system evolves linearly. So, the initial covariance matrices of the two spacecraft are propagated in the discretized time window through the use of the STM, obtained with a first-order DA expansion

$$\mathbf{C}_{p,i+1}^j = \mathbf{A}_{p,i+1}^j \mathbf{C}_{p,i}^j (\mathbf{A}_{p,i+1}^j)^T \quad i \in \{0, \dots, N-1\}. \quad (24a)$$

$$\mathbf{C}_{s,i+1} = \mathbf{A}_{s,i+1} \mathbf{C}_{s,i} \mathbf{A}_{s,i+1}^T \quad i \in \{0, \dots, N-1\}. \quad (24b)$$

In the case of the secondary, the STMs are independent of the optimization, and so they are constant throughout the major iterations. Using a first-order DA expansion, the Jacobian matrices of the nonlinear transformations from Eq. (4), $\mathbf{H}_{p,i}^j$ and $\mathbf{H}_{s,i} \in \mathbb{R}^{3 \times 6}$, are obtained. These are employed to compute the covariance of the Cartesian positions of the two spacecraft

$$\mathbf{P}_{p,i}^j = \mathbf{H}_{p,i}^j \mathbf{C}_{p,i}^j (\mathbf{H}_{p,i}^j)^T \quad i \in \{0, \dots, N\}, \quad (25a)$$

$$\mathbf{P}_{s,i} = \mathbf{H}_{s,i} \mathbf{C}_{s,i} \mathbf{H}_{s,i}^T \quad i \in \{0, \dots, N\}. \quad (25b)$$

In the case in which the propagation is performed using Cartesian elements, $\mathbf{H}_{p,i}^j = \mathbf{H}_{s,i} = [\mathbf{I}_3, \mathbf{0}_3; \mathbf{0}_{3 \times 6}]$. Since the states are assumed to be Gaussian, the covariance of the Cartesian relative position at each node is the sum of the covariances of the Cartesian position of the two spacecraft

$$\mathbf{P}_i^j = \mathbf{P}_{p,i}^j + \mathbf{P}_{s,i} \quad i \in \{0, \dots, N\}. \quad (26)$$

This 3×3 matrix defines a 3D ellipsoid that evolves in time and is pivotal in the computation of SMD and in the definition of the CAM scheme.

We stress the importance of updating the history of the covariance matrices of the primary spacecraft with each major iteration since a specific maneuver could significantly change the state transition between two nodes, leading to a different covariance. In particular, a maneuver could cause a stretch and/or a rotation of the covariance at node i with respect to the same node in the previous major iteration. According to Eq. (11), this could cause a SMD constraint to be violated in the node, thus requiring a different maneuver with respect to the previous major iteration.

C. Lossless Relaxation of the Control Magnitude Constraint

Equation (6e) is a non-convex equality constraint. Following the work from [42], we introduce a lossless relaxation to convexify the constraint: Eq. (6e) is transformed into an inequality constraint and the control magnitude is added to the optimization vector. In this way, Eq. (6e) becomes a second-order cone constraint. The variable u_i is now allowed to take values higher than the norm of the control that acts on the dynamics

$$u_i \geq \sqrt{u_{i,1}^2 + u_{i,2}^2 + u_{i,3}^2} \quad i \in \{0, \dots, N-1\}, \quad (27)$$

The discretized forms of Eq. (6a) and Eq. (6f) become respectively

$$J = \sum_{i=0}^{N-1} u_i, \quad (28)$$

$$0 \leq u_i \leq 1 \quad i \in \{0, \dots, N-1\}, \quad (29)$$

This relaxation is lossless, meaning that the optimal solution for the convexified problem is also optimal for the original problem.

D. Convexification of the Keep-Out-Zone Constraint

The primary goal of the maneuver is to reduce the collision risk by lowering IPoC. This objective is mathematically formulated using SMD by leveraging the method proposed by Mao *et al.* [43] and Armellin [7]. In the following discussion, the indexes j and i are dropped since one the process is repeated multiple times inside the same major iteration and for each node. A projection and linearization algorithm is utilized to convexify the nonlinear constraint in Eq. (16), as depicted in Fig. 4. This algorithm operates iteratively within the framework of minor iterations, denoted by the symbol k . For each node, the projection convex sub-problem aims to find the point on the surface of the ellipsoid that is closest to the relative position \mathbf{r}^{k-1} from the previous minor iteration.

With reference to Fig. 4, let the ballistic relative position of the primary spacecraft at a generic node i be \mathbf{r}^0 . A tangent plane is built on \mathbf{z}^1 , which is the point on the surface of the ellipsoid that is closest to \mathbf{r}^0 : the admissible region for the optimization, then, is the hemi-space identified by the plane. The optimized relative trajectory in node i after the first minor iteration is \mathbf{r}^1 , which is used as a starting point to repeat the projection and linearization process. This process is repeated until a tolerance on the difference in relative position between two consecutive iterations is met, i.e. $\|\mathbf{r}^k - \mathbf{r}^{k-1}\| \leq tol_m$. When $k = 1$, the value of \mathbf{r}^0 is the value of the last minor iteration of the previous major iteration. Additionally, if $j = 1$, \mathbf{r}^0 is the relative position of the ballistic trajectory.

The first part of the minor iterations process consists in the projection of the relative trajectory point \mathbf{r}^k onto the ellipsoid identified by \bar{d}_m^2 , i.e., the search for the closest point to \mathbf{r}^k belonging to the surface of the KOZ. To perform this operation, we solve a quadratic optimization problem. First of all it is convenient to diagonalize the covariance matrix. Let the dynamics used in the major convex problem be expressed in the \mathcal{B} reference frame (e.g., an ECI frame), then $\mathbf{r}_{\mathcal{B}}^{k-1} \in \mathbb{R}^3$ and $\mathbf{P}_{\mathcal{B}} \in \mathbb{R}^{3 \times 3}$ are respectively the mean value and the covariance matrix of the relative position multivariate random variable expressed in this frame. Using the covariance's eigenvalues matrix $\mathbf{D} = \text{diag}([\lambda_1 \lambda_2 \lambda_3])$ and the corresponding eigenvectors matrix \mathbf{V} , the problem is rotated into reference frame \mathcal{C} and scaled so that the covariance is transformed into the identity matrix $\mathbf{I}_3 \in \mathbb{R}^{3 \times 3}$:

$$\hat{\mathbf{r}}_C^{k-1} = \mathbf{D}^{-1} \mathbf{V}^T \mathbf{r}_{\mathcal{B}}^{k-1} \text{ and } \hat{\mathbf{P}}_C = \mathbf{I}_3. \quad (30)$$

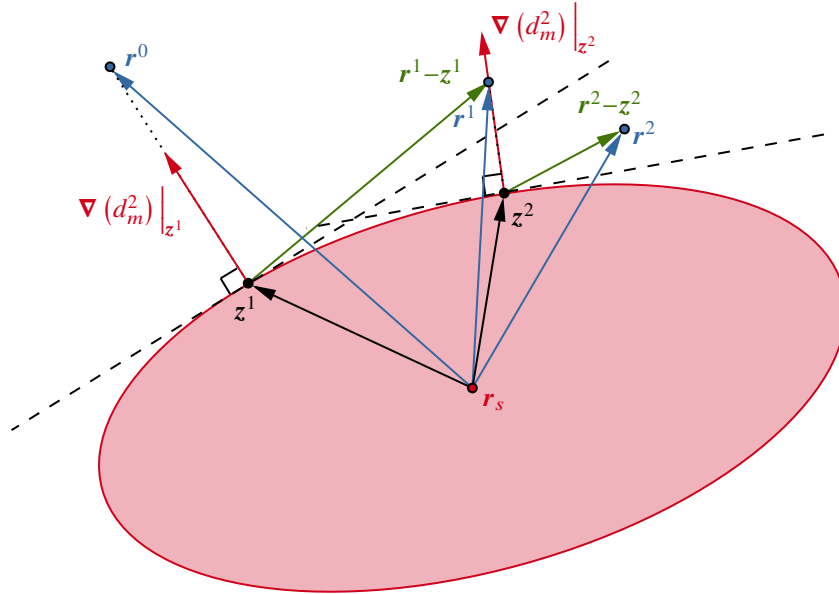


Figure 4 Simplified 2D version of the projection and linearization process for the generic node i .

Now, a simple quadratic optimization problem is solved in order to find the point \hat{z}_C

$$\min_{\hat{z}_C} \|\hat{z}_C^k - \hat{r}_C^{k-1}\| \quad (31a)$$

$$\text{s.t. } (\hat{z}_C^k)^T \hat{z}_C^k \leq \bar{d}_m^2, \quad (31b)$$

The objective Eq. (31a) minimizes the distance between the position of the previous iteration and the optimization variable \hat{z}_C . Eq. (31b) imposes a relaxed condition on the optimization variable to be inside the ellipsoid. This relaxed condition is lossless since the minimization of the objective guarantees that the optimization vector is always positioned on the surface of the ellipsoid, maximizing the distance from its center.

Once \hat{z}_C is determined, the solution is transformed back into the physical space using the equation $z_B^k = V D \hat{z}_C^k$. Now, the linearization of the KOZ constraint is performed on z^k . The dot product between the gradient of SMD computed on z^k and the vector going from z^k to the optimized trajectory point r^k must be positive. With the aid of Fig. 4, the constraint is employed by ensuring that the green red vectors both point outwards from the ellipsoid. The equation of the constraint in iteration k is (including also the indexes j and i)

$$\nabla(d_m^2)^{j,k} \Big|_{z_i^{j,k}} \cdot (r_i^{j,k} - z_i^{j,k}) \geq 0 \quad i \in \{1, \dots, N\}. \quad (32)$$

As highlighted by Malyyuta et al. [33], SCP algorithms can only converge if the initial trajectory guess is feasible with respect to the convex constraint, even if it does not comply with the nonlinear dynamics. In other words, the method described above only works if \hat{r}_C^{k-1} lies outside the region occupied by the ellipsoid volume for every node. Otherwise, if the ballistic relative trajectory point satisfies the inequality constraint in Eq. (31b), the relaxation fails because the objective function in Eq. (31a) becomes zero when $\hat{z}_C^k = \hat{r}_C^{k-1}$: this leads to Eq. (32) being undefined since the value of the gradient must be computed on the surface of the ellipsoid for it to be a relevant relaxation of the nonlinear constraint. So, for the nodes in which the original point is inside the ellipsoid, one should find a starting point (at major iteration j and minor $k = 0$) that satisfy Eq. (32), before applying the projection and linearization algorithm. A straightforward approach to address this issue is to use the point of intersection between the surface of the ellipsoid and the line connecting the ellipsoid's origin with the original point as the initial expansion point. In frame C , this point can be computed as follows

$$r_C^{j,0} = \left[\left(\frac{x}{\lambda_1} \right)^2 + \left(\frac{y}{\lambda_2} \right)^2 + \left(\frac{z}{\lambda_3} \right)^2 \right]^{-\frac{1}{2}} r_C^{j,0}, \quad (33)$$

where $r_C^{j,0}$ is the new point that might not satisfy the dynamics, $r_C^{j,0} = [x \ y \ z]^T$ is the original point inside the ellipsoid.

E. Squared Mahalanobis Distance Sensitivity Constraint

A typical solution of the long-encounter CA problem yields a IPoC profile, presenting at least one local maximum that is usually very close to \bar{P}_{IC} . If the gradient of SMD for these points is large, a small deviation from the optimized trajectory (for example, due to errors in the actuation of the maneuver) may cause the actual value of SMD to vary significantly. For this reason, it is chosen to introduce a constraint that bounds the value of the norm of the gradient of SMD for these nodes.

Let us assume that a solution of a major iteration $j - 1$ is available, then $P_{IC,i}^{j-1}$ is known for every node. The constraint on the gradient of SMD is applied at node i only if the following condition is fulfilled

$$P_{IC,i}^{j-1} \geq (1 - \varepsilon)\bar{P}_{IC}, \quad (34)$$

where $\varepsilon \in \mathbb{R}_{[0,1]}$ is an arbitrary percentage of the IPoC limit. This constraint bounds the norm of the gradient of SMD to be lower or equal to a certain limit λ

$$\text{if Eq. (34) is true,} \quad \|\nabla(d_m^2)_i\| \leq \gamma_i \quad i \in \{1, \dots, N\}. \quad (35)$$

The limit value of the gradient γ_i is computed according to the following procedure. Let the maximum allowed deviation of IPoC at a distance Δr (e.g. equal to the combined HBR) from \mathbf{r} be equal to or lower than a percentage of \bar{P}_{IC}

$$\Delta P_{IC,max} \leq \rho \bar{P}_{IC}, \quad (36)$$

where $\rho \in \mathbb{R}_{[0,1]}$ is a design parameter. The IPoC variation can be expressed as a function of the derivative of IPoC with respect to SMD and of the distance $d\mathbf{r}$ from the relative position \mathbf{r}

$$dP_{IC} = \frac{\partial P_{IC}}{\partial d_m^2} \nabla(d_m^2) \cdot d\mathbf{r}. \quad (37)$$

The derivative of IPoC is always negative because it is computed according to the approximation in Eq. (13)

$$\frac{\partial P_{IC}}{\partial d_m^2} = -\frac{P_{IC}}{2}. \quad (38)$$

To maximize the expression in Eq. (37), then, the deviation must be parallel and opposite to ∇d_m^2 and equal to Δr in magnitude:

$$d\mathbf{r} = -\Delta r \frac{\nabla(d_m^2)}{\|\nabla(d_m^2)\|}. \quad (39)$$

Substituting Eq. (39) and Eq. (38) into Eq. (37), one gets an explicit expression for the limit of the variation of IPoC

$$\Delta P_{IC,max} = \frac{P_{IC}}{2} \|\nabla(d_m^2)\| \Delta r. \quad (40)$$

Now, substituting Eq. (40) into Eq. (36) and rearranging, the limit imposed to ∇d_m^2 in Eq. (35) eventually depends on the value of IPoC

$$\gamma_i = \frac{2\rho \bar{P}_{IC}}{\Delta r P_{IC,i}} \quad i \in \{1, \dots, N\}. \quad (41)$$

The components of $\nabla(d_m^2)_i$ are 3 new optimization variables per node.

Since the expression of SMD is quadratic with respect to the relative position variable \mathbf{r}_i , its gradient is linear, and it reads

$$\nabla(d_m^2)_i = 2\mathbf{r}_i^T \mathbf{P}_i^{-1} \quad i \in \{1, \dots, N\}. \quad (42)$$

IV. Station-Keeping Constraints

The base SOCP presented in Section III is completed in this section by the translation of SK requirements into a linear constraints.

A. GEO Station-Keeping Constraint

Maneuvers in GEO orbits must consider the need to respect a SK constraint. The SK is viewed as a "keep-in box" in two dimensions, the longitude and the latitude of the spacecraft. The nonlinear dynamics of the evolution of the two geodetic variables are dependent only on the state of the primary spacecraft and on the time variable

$$\boldsymbol{\phi}(t) = \mathbf{g}(t, \mathbf{x}(t)), \quad (43)$$

where $\mathbf{g}(\cdot) : \mathbb{R}_{[t_0, t_f]} \times \mathbb{R}^6 \rightarrow \mathbb{R}^2$ is a function that first transforms the state into Earth Centered Earth Fixed (ECEF) and then into geodetic and $\boldsymbol{\phi} \in \mathbb{R}^2$ is the vector comprising latitude and longitude. After discretization, the perturbation in the state is given by Eq. (19a), where the expansion point is, as usual, the output of the previous major iteration ($\tilde{\mathbf{x}}_i^j = \mathbf{x}_i^{j-1}$).

Using DA, Eq. (43) is approximated as a first-order Taylor polynomial

$$\boldsymbol{\phi}_i^j = \mathcal{T}_{\boldsymbol{\phi}_i^j}^1(\mathbf{x}_i^j) \quad i \in \{1, \dots, N\}. \quad (44)$$

Equation (44) allows for the representation of the perturbation of the geodetic coordinates as a linear transformation of

the perturbation of the state

$$\delta \boldsymbol{\phi}_i^j = \mathbf{G}_i^j \delta \mathbf{x}_i^j \quad i \in \{1, \dots, N\}, \quad (45)$$

where $\mathbf{G}_i^j \in \mathbb{R}^{2 \times 6}$ is the linear map of the geodetic transformation for node i in major iteration j .

The SK requirement states that at all times, the latitude and longitude need to be inside a rectangular box which is centered on the nominal coordinates $\boldsymbol{\phi}_0 \in \mathbb{R}^2$; the sides of the box are the elements of $\Delta \boldsymbol{\phi} \in \mathbb{R}^2$

$$\boldsymbol{\phi}_0 - \Delta \boldsymbol{\phi} \leq \boldsymbol{\phi}_i^j \leq \boldsymbol{\phi}_0 + \Delta \boldsymbol{\phi} \quad i \in \{1, \dots, N\}, \quad (46)$$

where the symbol \leq indicates the componentwise inequality. Thus, rearranging Eq. (45) and Eq. (19a) and splitting the two inequalities, the linearized SK constraint can be written as two componentwise inequalities

$$\mathbf{G}_i^j \mathbf{x}_i^j \geq \boldsymbol{\phi}_0 - \Delta \boldsymbol{\phi} + \mathbf{d}_i^j \quad i \in \{1, \dots, N\}, \quad (47a)$$

$$\mathbf{G}_i^j \mathbf{x}_i^j \leq \boldsymbol{\phi}_0 + \Delta \boldsymbol{\phi} + \mathbf{d}_i^j \quad i \in \{1, \dots, N\}, \quad (47b)$$

where $\mathbf{d}_i^j = \mathbf{G}_i^j \mathbf{x}_i^{j-1} - \bar{\boldsymbol{\phi}}_i^j$ is the residual of the linearization. $\bar{\boldsymbol{\phi}}_i^j = \mathbf{g}(t_i, \bar{\mathbf{x}}_i^j)$ is the constant part of the geodetic transformation, i.e., the nonlinear function evaluation of the expansion point.

B. Station-Keeping State Targeting

A condition of return to the nominal orbit can be implemented setting the final target state of the optimization to be equal to the final state of the ballistic trajectory. Thus, a new bound constraint is introduced into the original convex problem, which bounds the state at the last node of the optimization:

$$\mathbf{x}_N + \mathbf{s}_T^+ - \mathbf{s}_T^- = \mathbf{x}_T, \quad (48)$$

where the variables \mathbf{s}_T^+ and $\mathbf{s}_T^- \in \mathbb{R}^6$ are slack variables used to create a soft constraint, and $\mathbf{x}_T = \mathbf{x}_N^0$. A trade-off between the pure CA and the pure SK maneuvers can be obtained adding a term to the objective function. The weight κ_T determines the softness of the constraint

$$J_T = \kappa_T \|\mathbf{s}_T^+ + \mathbf{s}_T^-\|_1 \quad (49a)$$

$$\mathbf{s}_T^+, \mathbf{s}_T^- \geq 0, \quad (49b)$$

In LEO scenarios, the return to the nominal orbit can be considered a sufficient station keeping requirement, but the same is not valid for GEO orbits.

For GEO orbits, finding the target state \mathbf{x}_T to minimize the violation of the SK box is the typical optimization problem of the periodic SK maneuvers. Analytical solutions exist when only the first harmonics of the gravity potential are considered. In contrast, classical nonlinear optimization methods can solve the problem numerically when more perturbations are considered. To overcome the long computational time required by the latter method, a SCP formulation is presented, where the dynamics are dealt with using the method presented in Section III.A. The objective of the optimization is to maximize the time spent inside the SK box during a period $t \in \mathbb{R}_{[t_f, t_f + \gamma]}$ where t_f is the final time of the CA window and γ is the length of the time frame before executing another SK maneuver. The time window is discretized in the usual way into $M + 1$ equally spaced nodes. After the discretization, it is straightforward to define the dynamics constraint for the state of the satellite in a very similar way to Eq. (22). In this case, the initial state must remain unconstrained and no control is acting

$$\mathbf{x}_{i+1}^j - \mathbf{A}_{i+1}^j \mathbf{x}_i^j = \mathbf{c}_i^j \quad i \in \{0, \dots, M\}, \quad (50)$$

Where $\mathbf{A}_{i+1}^j \in \mathbb{R}^{6 \times 6}$ is the STM and $\mathbf{c}_i^j = \bar{\mathbf{x}}_{i+1}^j - \mathbf{A}_{i+1}^j \tilde{\mathbf{x}}_i^j$ is the residual of the linearization. The SK constraint is enforced similarly to that of Eq. (47). In this problem the control is not available in every node to adjust the position of the spacecraft, so it is unavoidable that, in a long period of propagation (e.g., two weeks), the orbital perturbations make the satellite violate the SK box. The constraint is then enforced as a soft constraint via the introduction of $2 \times (M + 1)$ vector slack variables (each comprising two elements, which influence longitude and latitude respectively), χ_i^+ and $\chi_i^- \in \mathbb{R}^2$. These variables quantify the entity of the violation of the SK box requirement over each node

$$\mathbf{G}_i^j \mathbf{r}_i^j + \chi_i^+ \geq \phi_0 + \mathbf{d}_i^j - \Delta \phi \quad i \in \{0, \dots, M\}, \quad (51a)$$

$$\mathbf{G}_i^j \mathbf{r}_i^j - \chi_i^- \leq \phi_0 + \mathbf{d}_i^j + \Delta \phi \quad i \in \{0, \dots, M\}, \quad (51b)$$

where $\mathbf{d}_i^j = \mathbf{G}_i^j \mathbf{r}_i^{j-1} - \bar{\phi}_i^j$ is the usual residual of the linearization. The slack variables need to be non-negative

$$\chi_i^+, \chi_i^- \geq 0 \quad i \in \{0, \dots, M\}, \quad (52)$$

The optimization minimizes these violations by acting only on the initial state of the propagation. Thus the objective function is

$$J_T = \sum_{i=0}^M \|\chi_i^+ + \chi_i^-\|_1. \quad (53)$$

The optimization problem can be summarized as

$$\min_{\mathbf{x}_0} \text{Eq. (53)}, \quad \text{s.t. Eqs. (50) to (52)} \quad (54)$$

V. Finalization of the SOCP

In order to finalize the SOCP, a trust region algorithm combined with virtual controls is introduced.

A. Trust Region Constraint

The use of a trust region algorithm is of pivotal importance when dealing with a complexly nonlinear problem that has been linearized. The classic approach introduces a node-wise constraint that bounds the norm of the maximum deviation allowed to the state variables with respect to the linearization point. The radius of the trust region is usually proportional to some performance index that is related to how well the linearized dynamics represent the actual non-linear problem [33]. Here we introduce a methodology that adjusts the trust region radius for every single variable according to a measure of its nonlinearity and uses a limited number of parameters to update the radius.

The idea for this algorithm stems from the work of Losacco *et al.* on the nonlinearity index (NLI) [34] and the one of Bernardini *et al.* on trust region [35]: a second-order Taylor expansion of the nonlinear dynamics is computed using DA. This allows one to obtain the first-order expansion of the Jacobian of the constraints with respect to the optimization variables (both the states and controls):

$$\mathbf{J}_i = \bar{\mathbf{J}}_i + \delta\mathbf{J}_i \quad i \in \{1, \dots, N\}, \quad (55)$$

where $\mathbf{J}_i \in \mathbb{R}^{6 \times 9}$. From now on, in this section, the index i will be dropped for readability; still, the equations are valid for each node.

The deviation of the Jacobian is a first-order function of the deviation of the optimization variables

$$J_{uv} = \bar{J}_{uv} + \delta J_{uv} = \bar{J}_{uv} + \sum_{w=1}^9 a_{uvw} \delta x_w \quad u \in \{1, \dots, 6\} \quad v \in \{1, \dots, 9\}, \quad (56)$$

where $\delta x_w = x_w - \bar{x}_w$ is the componentwise deviation from the reference variable, which comprises both the state and the control: $w \in \{1, \dots, 6\}$ indicates the state components, $w \in \{7, \dots, 9\}$ the control.

The component-wise NLI is defined as

$$\nu_w = \sqrt{\frac{\sum_{u=1}^6 \sum_{v=1}^9 a_{uvw}^2}{\sum_{u=1}^6 \sum_{v=1}^9 \bar{J}_{uv}^2}} |\delta x_w| = \xi_w |\delta x_w|. \quad (57)$$

The variable $\xi_w \in \mathbb{R}_{\geq 0}$ is a measure of the nonlinearity of the reference solution; $\nu_w \in \mathbb{R}_{\geq 0}$ is an indicator of the nonlinearities for a variation δx_w from the reference. To allow variations within the accuracy of the linearizations, ν_w is bounded by a maximum value $\bar{\nu}$:

$$\nu_w = \xi_w |\delta x_w| \leq \bar{\nu} \quad w \in \{1, \dots, 9\}, \quad (58)$$

Making the absolute value explicit and bringing the optimization variables to the left, Eq. (58) translates into two trust region constraints [†]

$$\xi_i \odot [\mathbf{x}_i^T \mathbf{u}_i^T]^T \leq \xi_i \odot [\tilde{\mathbf{x}}_i^T \tilde{\mathbf{u}}_i^T]^T + \bar{v} \cdot \mathbf{1} \quad i \in \{1, \dots, N\}, \quad (59a)$$

$$\xi_i \odot [\mathbf{x}_i^T \mathbf{u}_i^T]^T \geq \xi_i \odot [\tilde{\mathbf{x}}_i^T \tilde{\mathbf{u}}_i^T]^T - \bar{v} \cdot \mathbf{1} \quad i \in \{1, \dots, N\}, \quad (59b)$$

where \mathbf{x}_i and \mathbf{u}_i are the state and control to be optimized, $\tilde{\mathbf{x}}_i$ and $\tilde{\mathbf{u}}_i$ are the expansion points, $\xi_i = [\xi_{i1}, \xi_{i2}, \dots, \xi_{i9}]^T$, $\mathbf{1} \in \mathbb{R}^9$ is a vector of ones, and the symbol \odot indicates the Hadamard product; the index i is used again to indicate the node-wise constraints. For $i = 0$ no deviation is allowed so the constraint is not set as it would be redundant with Eq. (23).

1. Virtual Controls

The introduction of the trust region constraint can cause artificial infeasibility, so virtual controls, and virtual buffers are added to the dynamics, CA, SK, and ∇d_m^2 constraints, which improve the convergence of the method. The new constraints with virtual controls become

$$\mathbf{x}_{i+1}^j - \mathbf{A}_{i+1} \mathbf{x}_i^j - \mathbf{B}_{i+1}^j \mathbf{u}_i^j + \mathbf{v}_{dyn,i+1}^j = \mathbf{c}_i^j \quad i \in \{0, \dots, N-1\}, \quad (60a)$$

$$\nabla (d_m^2)^{j,k} \Big|_{\mathbf{z}_i^{j,k}} \cdot (\mathbf{r}_i^{j,k} - \mathbf{z}_i^{j,k}) + \mathbf{v}_{ca,i}^j \geq 0 \quad i \in \{1, \dots, N\}, \quad (60b)$$

$$\mathbf{G}_i^j \mathbf{x}_i^j + \mathbf{v}_{sk,i}^j \geq \phi_0 - \Delta\phi + \mathbf{d}_i^j \quad i \in \{1, \dots, N\}, \quad (60c)$$

$$\mathbf{G}_i^j \mathbf{x}_i^j + \mathbf{v}_{sk,i}^j \leq \phi_0 + \Delta\phi + \mathbf{d}_i^j \quad i \in \{1, \dots, N\}, \quad (60d)$$

$$\|\nabla (d_m^2)_i\| + \mathbf{v}_{s,i}^j \leq \gamma_i \quad i \in \{1, \dots, N\}, \quad (60e)$$

where $\mathbf{v}_{dyn,i}^j \in \mathbb{R}^6$ is the virtual control vector, $\mathbf{v}_{ca,i}^j \in \mathbb{R}$ is the virtual buffer for the SMD constraint, $\mathbf{v}_{sk,i}^j \in \mathbb{R}^2$ is the virtual buffer for the station keeping constraint, and $\mathbf{v}_{s,i}^j \in \mathbb{R}$ is the virtual buffer for the SMD sensitivity constraint.

Ideally, the virtual controls should all go to 0 at convergence, so a second-order cone constraint is built on each node, and in the objective function, a term is added which is proportional to it; the value of the weight in the objective function should be orders of magnitude higher than the one on the control, e.g., 10^4 , to favor the penalization of the virtual control variables

[†]It is important to have ξ_{iw} in the numerator, otherwise when $\xi_{iw} = 0$ (linear dynamics) the constraint would become undefined.

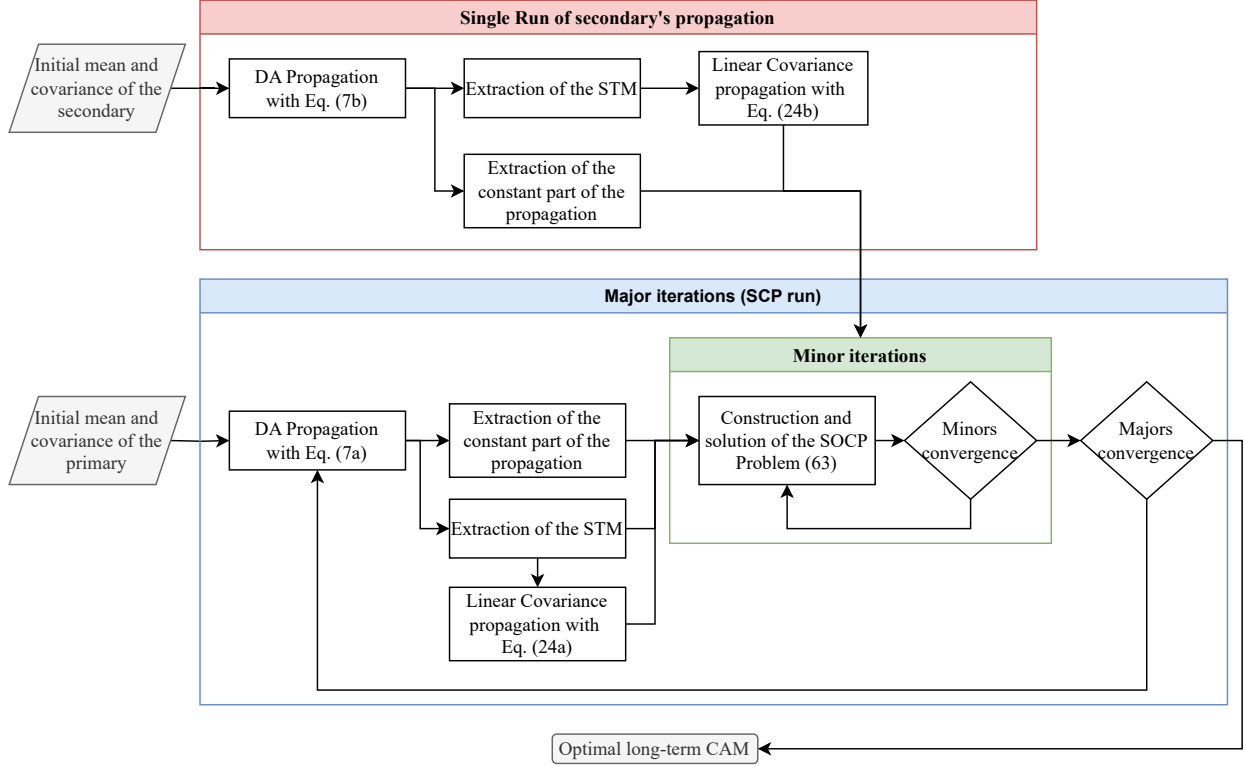


Figure 5 High-level flowchart of the SCP iterative process.

$$v_i \leq \sqrt{(v_{s,i}^j)^2 + (v_{ca,i}^j)^2 + \|v_{dyn,i}^j\| + \|v_{sk,i}^j\|} \quad i \in \{1, \dots, N\}, \quad (61a)$$

$$J_{vc} = \kappa_{vc} \sum_{i=0}^N v_i, \quad (61b)$$

B. Final Form of the SOCP

The final objective function is given by the sum of Eq. (28), Eq. (49a), and Eq. (61b):

$$J = \kappa_T \|s_T^+ + s_T^-\|_1 + \kappa_{vc} \sum_{i=0}^N v_i + \sum_{i=0}^{N-1} u_i. \quad (62)$$

The full convex optimization problem with the novel constraints (SK and SMD sensitivity) is summarized in Problem (63).

$$\begin{aligned} \min_{\mathbf{x}, \mathbf{u}} \quad & \text{Eq. (62)} \\ \text{s.t.} \quad & \text{Eqs. (23), (27), (29), (42), (48), (49b), (59), (60a) to (60c), (60e) and (61a)} \end{aligned} \quad (63)$$

In Fig. 5 and in Appendix A, a schematics and the algorithmic representation of the method are reported, respectively.

VI. Results

In this section, we study a LEO, a GEO and a HEO scenario: the effect of different parameters and constraints is analyzed to determine how they affect the computed optimal CAM thrust profile. In particular, we will analyze the following factors: risk metric, maximum thrust, and inclusion of operational constraints (SK and ∇d_m^2). The simulations are run with MATLAB r2022b on AMD Ryzen 9 6900HS @ 3.3GHz. The optimization is performed using MOSEK 10.0.24, which implements a state-of-the-art primal-dual interior point solver. In all the considered test-cases, the nominal TCA is assumed to happen the 2nd of March 2015 at 06:00:00 A.M. .

Despite the algorithm working with a low-thrust formulation, i.e., integrating the control acceleration, it was chosen to display the corresponding Δv in the figures, as it is an easier-to-understand quantity, and the mass loss due to the propulsion is neglected. The Δv is obtained by integrating the acceleration over the time step: $\Delta v_i = \mathbf{u}_i \Delta t$.

A. LEO Scenario

The LEO scenario is based on the set of test cases reported in [9]. In Table 1, the physical properties of the spacecraft are shown, and in Table 2 we report the orbital parameters at TCA. The simulations are run for two orbital periods with TCA as the median point of the propagation; the time nodes previous to TCA are negative, and the ones after are positive. Each orbital period is discretized into 60 nodes, granting a minimum thrust arc of 3 deg and a total of 120 available thrusting opportunities. The propulsion system is chemical, and can achieve a maximum thrust of 1 N, which corresponds to a maximum acceleration of 5 mm/s² for a mass of 200 kg. In the following, the simulations in which the maximum acceleration is 5 mm/s² will be referred to as *high-thrust*, as opposed to the *low-thrust* ones, in which the maximum acceleration is much lower. In both cases, the maneuvers are modeled as finite burns.

In Table 3, the covariance at TCA is expressed in the radial, along-track, cross-track (RTN) reference frame of the two spacecraft. Before summing them, the two covariance matrices must be expressed in a common reference frame, e.g., ECI.

Table 1 LEO scenario: physical properties of the spacecraft.

Spacecraft	m [kg]	A_{drag} [m ²]	C_D [-]	A_{SRP} [m ²]	C_r [-]	HBR [m]
Primary	200	1	2.2	1	1.31	25
Secondary	50	0.05	2	0.05	1.31	7

Table 2 LEO scenario: orbit parameters at TCA.

Spacecraft	a [km]	e [-]	i [deg]	ω [deg]	Ω [deg]	θ [deg]
Primary	6800	0	0	0	0	0
Secondary	6802	4.42×10^{-4}	8.4×10^{-5}	1.9103	0	-1.9103

Table 3 LEO scenario: diagonal elements of the covariance at TCA.

Spacecraft	C_{rr} [m ²]	C_{tt} [m ²]	C_{nn} [m ²]	$C_{\dot{r}\dot{r}}$ [m ² /s ²]	$C_{\dot{t}\dot{t}}$ [m ² /s ²]	$C_{\dot{n}\dot{n}}$ [m ² /s ²]
Primary	0.625	10	3.025	0.00625	0.05625	0.00225
Secondary	5.625	90	27.225	0.05625	0.50625	0.02025

1. Comparison of Risk Metrics

The selection of different risk metrics determines different optimal maneuvers. The chosen risk thresholds are $\bar{P}_{IC} = 10^{-6}$, $\bar{P}_{IC,m} = 10^{-4}$, and $\bar{d}_{miss} = 2$ km. Fig. 6 makes it clear that when the IPoC metric is used, the computed maneuver is mostly out-of-plane, whereas it is tangential in the other two cases. The less restrictive metric in terms of total Δv is $P_{IC,m}$, which requires 183 mm/s. The evolution of $P_{IC,m}$ of the ballistic trajectory envelops IPoC, as shown in Fig. 7a, guaranteeing that the former is a very conservative estimate of the latter. The most demanding metric, instead, is d_{sep} , with a two-firings Δv of 387 mm/s: to avoid the sphere of 2 km centered in the secondary spacecraft, the tangential maneuver is the most efficient, as expected from the short-term problem [8, 44]. Most notably, as already suggested in [9], the d_{sep} metric in Fig. 7b exhibits an opposite behavior with respect to IPoC and $P_{IC,m}$: the evolution of the covariance in the probability-based criteria determines a high risk in the period in which the relative distance between the two objects is higher.

2. Comparison of Thrust Systems

The same scenarios of the previous section are analyzed using a low-thrust system with a maximum thrust of 50 mN, corresponding to a maximum acceleration of 0.25 mm/s². In Fig. 6 the maneuvers of the different cases are shown. In the IPoC case, the total Δv required is 330 mm/s, in the $P_{IC,m}$ case it is 185 mm/s and in the d_{sep} case 407 mm/s. The number of total nodes where thrust is active increases in the three cases from the 2 of the high-thrust system to 13, 7, and 15 for the low-thrust system. As expected from a fuel-optimal low-thrust solution, the optimizer achieves a bang-bang profile, and the firing windows overlap with the short firings produced by the high-thrust system.

3. Return to the Nominal Orbit

After completing reducing the collision risk, it might be required to the primary spacecraft to return to its nominal orbit. This is obtained by constraining the optimized final state to match the final state of the ballistic trajectory. So, in Eq. (48), $\mathbf{x}_T = \mathbf{x}_N^0$. The two trajectories, with and without return constraints, are shown in Fig. 8b. The thrust profile in Fig. 8a should be compared with the one in Fig. 6b, which is the corresponding scenario with no return constraint. The first firing is substantially the same, with only a slight modification in the direction of the thrust (radial and along-track components). All of the following firings are used to reroute the spacecraft toward the desired final state. The total Δv increases to 733 mm/s.

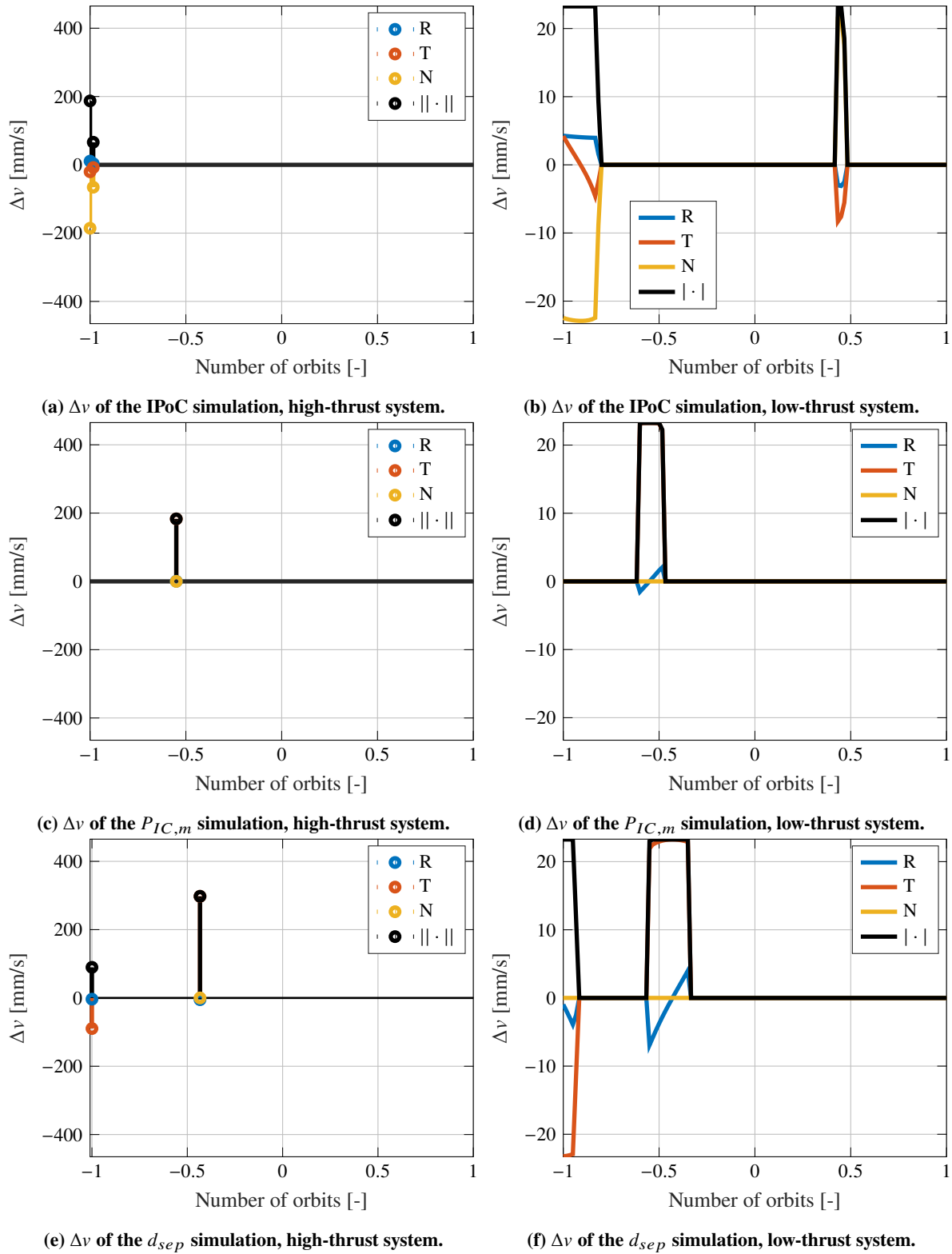
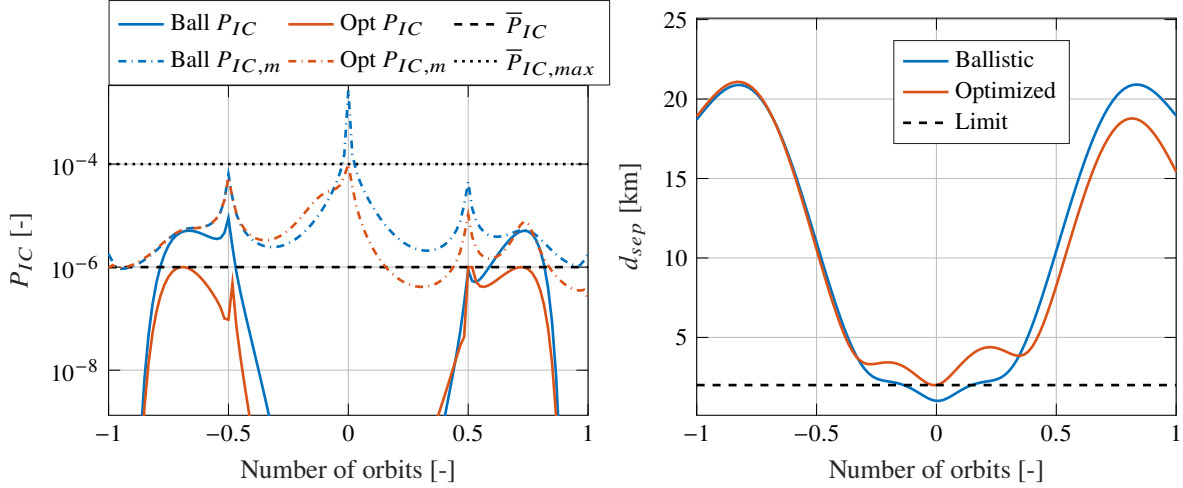


Figure 6 LEO scenario: Δv for different collision metrics and propulsion systems.

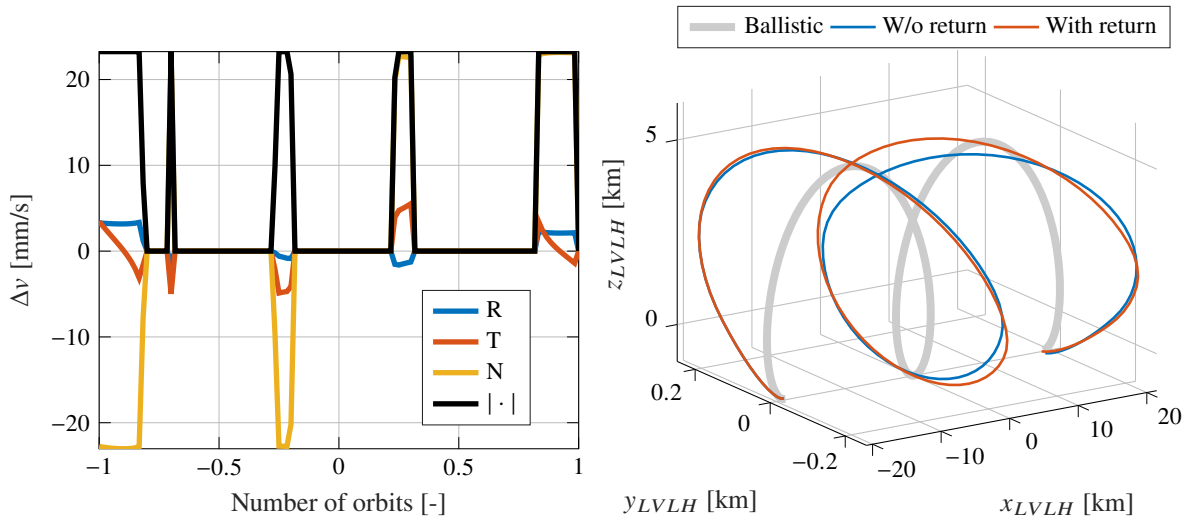


(a) P_{IC} and $P_{IC,m}$ of the ballistic and optimized trajectories. (b) d_{sep} of the ballistic and optimized trajectories.

Figure 7 LEO scenario: collision metrics comparison.

4. Squared Mahalanobis Distance Sensitivity Constraint

A scenario starting from TCA and spanning the period of 1 orbit is used to analyze the influence of the SMD sensitivity constraint on the maneuver. In Fig. 9a, IPoC for the cases with and without the SMD sensitivity constraint are shown. In Fig. 9a a zoom of the region in which the IPoC of the ballistic trajectory is over the limit is shown. The maximum value of IPoC happens at 0.73333 orbits from TCA. All four maneuvers have the effect of lowering the IPoC maximum value to 10^{-6} ; the increasingly constraining value of $\bar{\Delta P}_{IC}$, though, bounds ΔP_{IC} to increasingly lower values. Note that the SMD sensitivity constraint is applied only at 0.73333 orbits, since it is the only node in which IPoC is high enough to trigger its activation. Indeed, in Fig. 9b, ΔP_{IC} computed in the direction opposite to ∇d_m^2



(a) Δv of the return trajectory.

(b) Relative trajectory without and with return constraint.

Figure 8 LEO scenario: case with the return to the nominal orbit constraint.

respects the limit in all cases. This limit is respectively 4×10^{-7} , 3×10^{-7} , 2×10^{-7} , and 10^{-7} .

The total Δv required with the constraint's introduction increases when the safety margin increases. From the unconstrained case to the case with $\rho = 0.1$, the Δv goes from 257 to 265, 387, 507, and 580 mm/s. The maneuver is always a single-firing applied at the first node and the tangential component becomes more and more dominant.

B. GEO Scenario

A GEO test case is used to demonstrate the effectiveness of the SCP algorithm in another orbital regime. Simulations are performed considering a high thrust of 2.5 N, which corresponds to a maximum acceleration of 5 mm/s^2 for a 500 kg spacecraft. The orbital period is discretized into 60 nodes, so the maximum impulsive Δv between successive nodes is 7.18 m/s. For the low-thrust system the maximum thrust is 2.5 mN, i.e. a maximum acceleration of $5 \text{ } \mu\text{m/s}^2$.

In Table 4, the orbital parameters of the two spacecraft at TCA are represented. The two orbits are close to a perfect GEO, with a slight inclination and a difference in the semi-major axis of 1.5 km. The covariance of the two spacecraft is the same as in Table 3. In Table 5 the physical properties of the spacecraft are shown. The only relevant perturbations in the GEO regime are higher order gravitational harmonics, SRP, and third body attraction, so no information is required on the equivalent drag surface area and C_D coefficient.

In Fig. 10, the evolution of the three collision metrics for the considered scenario are presented. Similarly to the LEO scenario, $P_{IC,m}$ always provides an upper boundary to IPoC. Contrarily to the LEO scenario, in this case IPoC is close to the maximum when d_{sep} is close to the minimum. In general, all the computed maneuvers can easily lower the required risk metric.

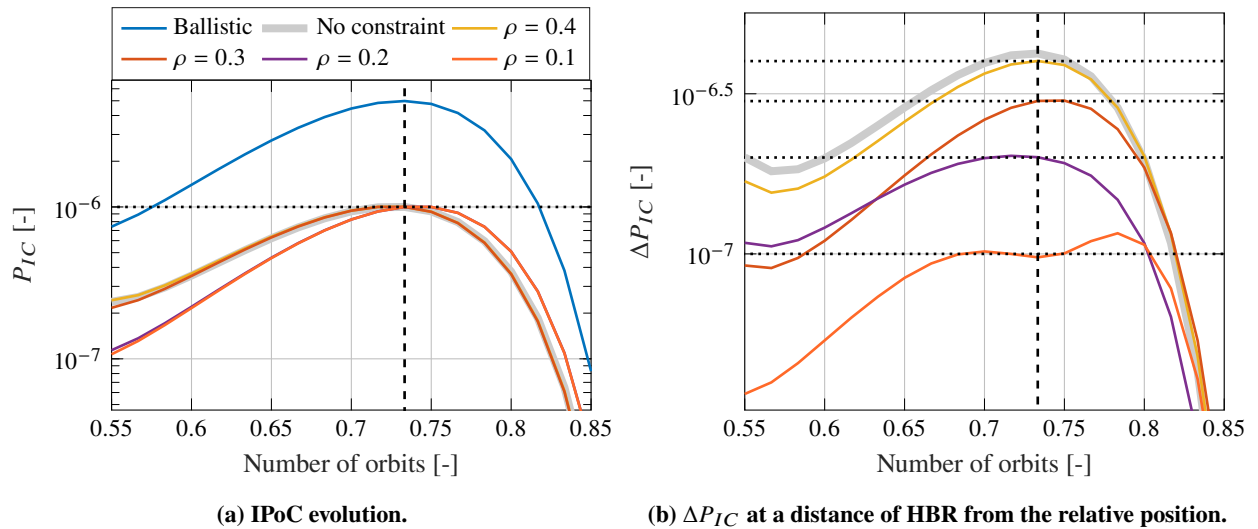


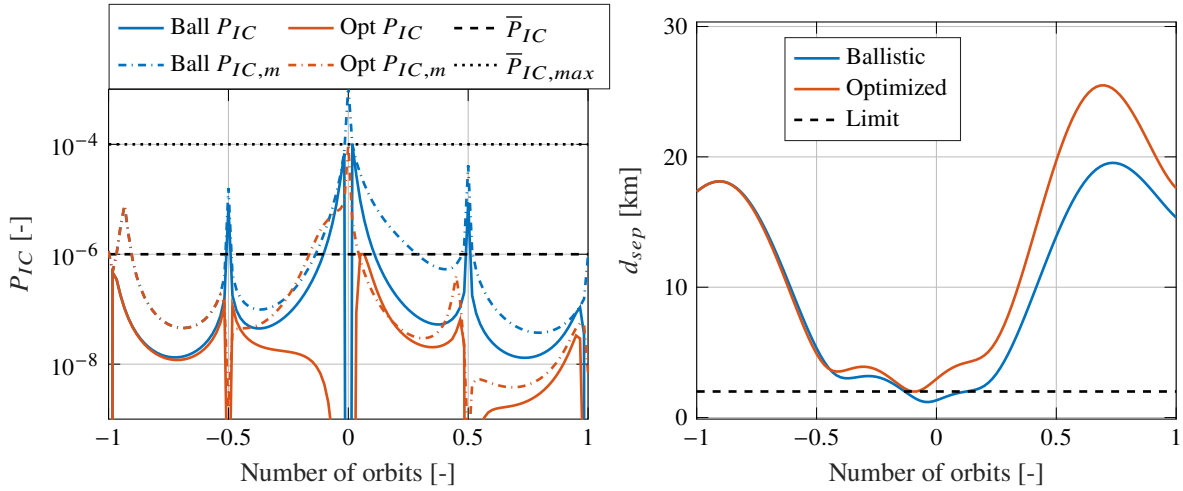
Figure 9 LEO scenario: collision metrics for cases with the sensitivity constraint.

Table 4 GEO scenario: orbit parameters at TCA.

Spacecraft	a [km]	e [-]	i [deg]	ω [deg]	Ω [deg]	θ [deg]
Primary	42166.025929	5.6×10^{-5}	0.118864	241.585377	76.181310	119.443522
Secondary	42167.765854	1.118×10^{-4}	0.118860	268.823470	76.181269	92.207487

Table 5 GEO scenario: physical properties of the spacecraft.

Spacecraft	m [kg]	A_{SRP} [m ²]	C_r [-]	HBR [m]
Primary	500	1	1.31	35
Secondary	200	1.2	1.31	10



(a) IPoC and $P_{IC,m}$ of the ballistic and optimized trajectories. (b) d_{sep} of the ballistic and optimized trajectories.

Figure 10 GEO scenario: collision metrics comparison.

1. Station-Keeping Constraint and Targeting

The primary spacecraft is commanded to always stay inside the latitude-longitude SK square box of side $\Delta\phi = 0.05$ deg around the nominal values of latitude (0 deg) and longitude (-155.08 deg). Moreover, the optimal final state target is computed so that the SK requirement is respected by the natural motion of the satellite for the following 14 days. This requirement is respected as shown in Fig. 11. For comparison, a scenario in which the SK constraint is not enforced is also reported in Fig. 11; in that case the maneuver causes an even more serious drift on the longitude than that of the ballistic trajectory.

The SK constraint completely changes the direction of the maneuver. In fact, the SK maneuver is mostly an out-of-plane correction of the inclination, which allows keeping the latitude inside the box [45]. The pure CAM in Fig. 12b, instead, is an almost purely tangential maneuver. Also, the entity of the total Δv is significantly changed by the constraint, going from 52 mm/s in the pure CAM case to 409 mm/s in the case with SK. Given the predominance of the SK constraint, the maneuver is only slightly modified by the use of different collision metrics: Fig. 12c and Fig. 12d

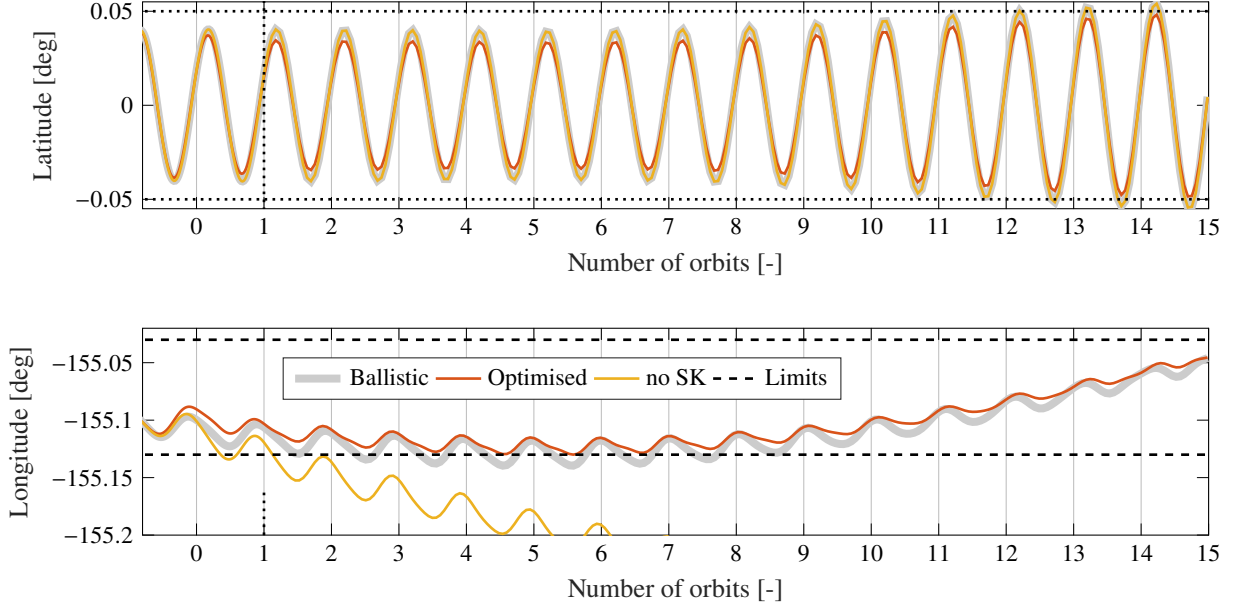


Figure 11 GEO scenario: latitude and longitude evolution with and without the SK requirement.

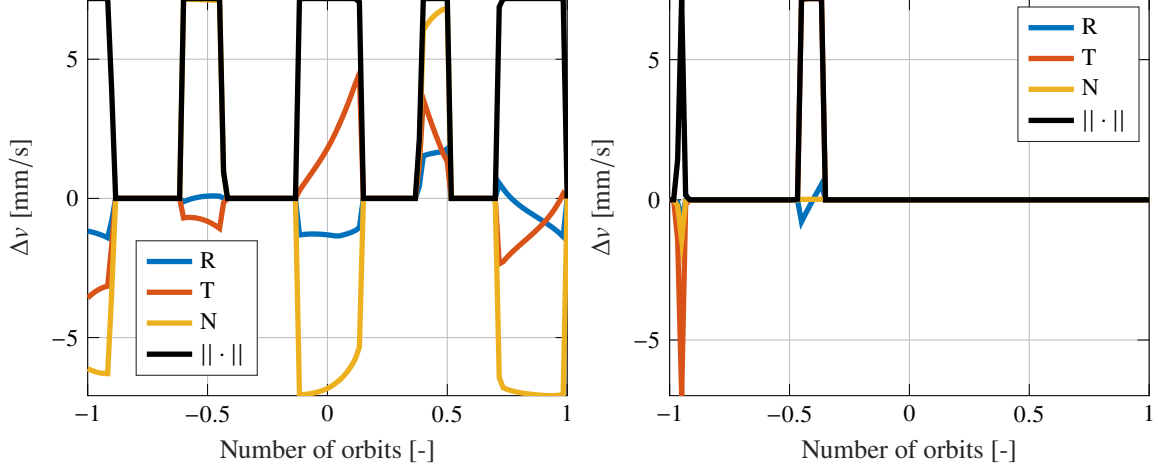
are very similar to Fig. 12a; the total Δv for the case with $P_{IC,m}$ is 366 mm/s and for the case with d_{sep} is 364 mm/s.

2. Squared Mahalanobis Distance Sensitivity Constraint

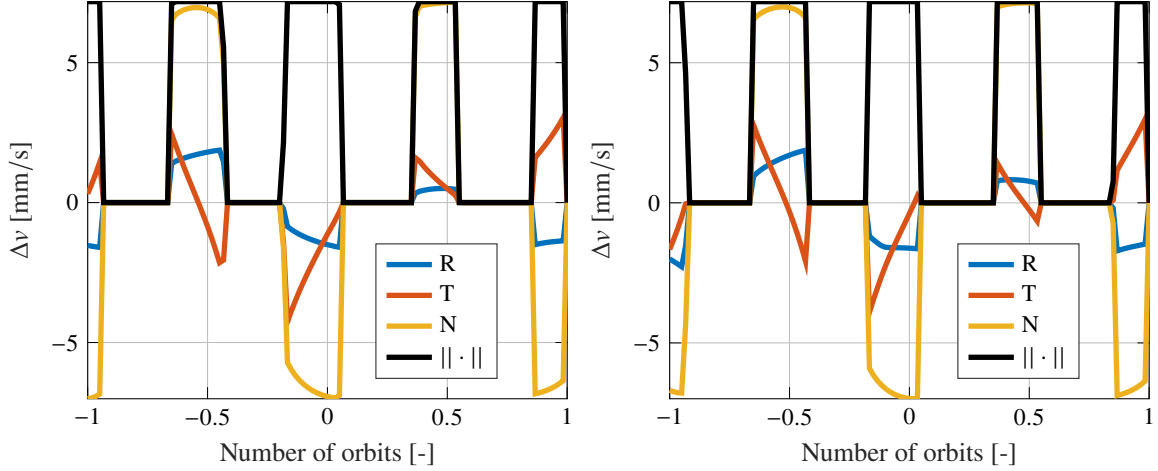
The SMD sensitivity constraint is applied to a GEO case with no SK target. The inclusion of the constraint completely shifts the maneuver. While in The SOCP does not guarantee to find the global optimum of the original OCP because the found solution could fall in a local optimum well. In fact, counter-intuitively the Δv required by the robust maneuver is lower than the one where the constraint was not applied (37 mm/s vs 51 mm/s). As pointed out in [7], the SOCP can only recover a local optimum solution depending on the initial reference solution. In other words, if a higher-cost solution falls closer to the initial ballistic trajectory, the solver is likely to find it and miss the global optimum. Nonetheless, the solver can still recover the optimal solution that is found in the case where the sensitivity constraint is employed. If the solution of the case with the sensitivity constraint is taken as reference and the SOCP is run without the constraint, the solution found is close to the reference, with a slightly lower Δv , 34 mm/s.

C. HEO scenario

The last test case that we analyze is the HEO scenario that was proposed as test case 9 in reference [41]. To validate the method, the same dynamical model used in [21], so we employ purely Keplerian dynamics. We refer to the original article for the data of the conjunction. This test case is used to validate the method against the solution obtained by Serra *et al.* [21] who impose a IPoC threshold of 10^{-4} . They obtain a four-impulses solution, with a total Δv of 4.380 mm/s. Our method recovers a solution that employs a single firing in the first node with RTN components equal to



(a) Δv of the IPoC simulation, low-thrust system. (b) Δv of the IPoC simulation with no SK, low-thrust system.



(c) Δv of the $P_{IC,m}$ simulation, low-thrust system. (d) Δv of the d_{sep} simulation, high-thrust system.

Figure 12 GEO Scenario: Δv for different collision metrics and propulsion systems.

$\Delta v = [-0.250, -0.128, 0.018]^T$ mm/s, and magnitude $\Delta v = 0.282$ mm/s. So, our method can obtain a single-firing solution which is twenty times lower than the reference. Note that to compute this maneuver, the SMD threshold method based on the cuboid IPoC approximation is used, because the constant IPoC approximation is not accurate, as shown in Section II.C.1. In Fig. 13, the evolution of the ballistic and optimized IPoC profile is shown: The optimized maneuver can lower IPoC according to the requirement.

D. Convergence and Analysis of the Solutions

This section analyzes the convergence properties of the SCP. In all the simulations presented in this work, the value of \bar{v} was 10^{-4} for all scenarios. This value is low because we expect the CAM to deviate from the original orbit by a small amount. For all the simulations, the tolerance for the convergence of the major iterations $tol_M = 10^{-3}$ and the one for the minor iterations is $tol_m = 10^{-6}$. The major iterations error is computed as the maximum difference between the

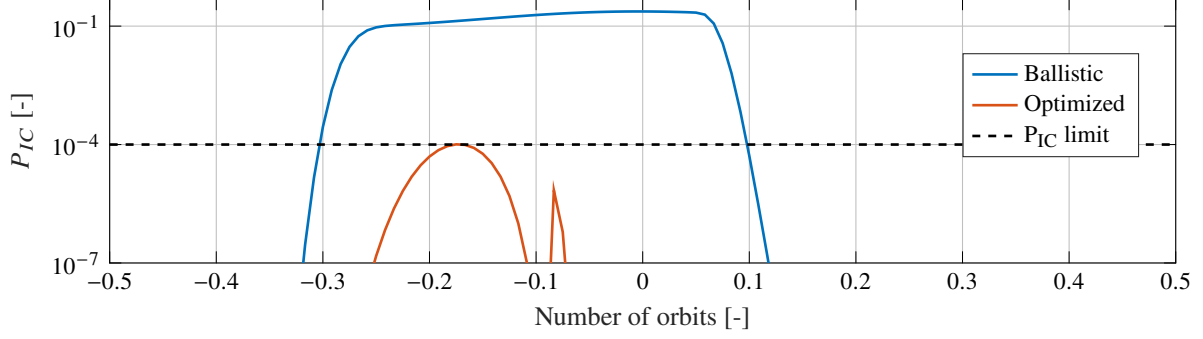


Figure 13 HEO Scenario: IPoC profile computed with the cuboid approximation.

Table 6 Convergence properties of the simulations.

sim n	n_{orb} [-]	orbit	SK	Thrust	∇d_m^2	n_{maj} [-]	n_{min} [-]	e [mm]	τ [s]
1	2	LEO	No	High	No	3	11	1.28	15.09
2	2	LEO	Yes	High	No	3	9	0.31	14.29
3	2	LEO	No	Low	No	3	9	17.54	13.92
4	2	LEO	Yes	Low	No	3	9	1.426	13.69
5	1	LEO	No	High	No	3	8	0.61	7.09
6	1	LEO	No	High	Yes	4	12	11.88	9.11
7	2	GEO	No	High	No	2	6	7.36	2.84
8	2	GEO	No	Low	No	2	5	3.33	2.59
9	2	GEO	Yes	High	No	2	9	2.66	18.31
10	2	GEO	Yes	Low	No	3	6	56.43	18.03
11	2	GEO	Yes	High	Yes	7	40	71.12	23.6
12	1	GEO	No	High	No	2	6	0.129	3.62
13	1	GEO	No	High	Yes	6	51	21.32	31.07
14	1	HEO	No	Low	No	3	5	0.168	2.3

control action of iteration j and that of iteration $j - 1$. The control action is always normalized with respect to the maximum control so that $0 \leq \|u_i\| \leq 1$. In this way, the entity of the error is independent of the maximum control and the major iteration tolerance does not need to be adjusted as a function of u_{max} . The minor iteration error is the maximum difference between the optimized relative position of two consecutive minor iterations. A complementary condition to reach convergence is the minimization of the sum of the virtual controls below a threshold of 10^{-7} , which is achieved in all simulations before the third major iteration.

In Table 6, the convergence results for the test cases analyzed are reported. The number of major iterations used to linearize the dynamics is always kept below 7, showing that the executed maneuvers are typically small and the deviation from the ballistic trajectory is almost negligible on an orbital scale. The trend indicates that the number of iterations is proportional to the length of the propagation window. Lastly, in LEO, the use of the SK targeting constraint

improves the convergence because the first reference solution already satisfies the constraint, whereas the same cannot be observed for GEO cases. The execution time τ is proportional to the number of minor iterations. More than 89% of the run time is required by the linearization of the dynamics and the building of the linear maps; on average, the solution of the convex problem only requires around 10% of the total run time. It is worth noticing that the accurate models greatly increase the computational time required by the propagation. For example, if the atmospheric model is not considered, the run time can be brought down to 2 s for the simulations in LEO. Indeed, in the GEO simulations, where the atmosphere model is not needed, the run times are typically shorter. They only get longer when the computation of the optimal target state is performed using Problem (54). As a last remark, we note that the implementation of the code is not optimized for speed, and it is the authors' opinion that the time to find a solution could be reduced by one order of magnitude at least if a more suitable implementation was used.

VII. Conclusions

A sequential convex program (SCP) was developed to design fuel-optimal collision avoidance maneuvers in long-term encounters. The original non-convex optimal control problem is locally approximated into a second-order cone program (SOCP), and the solution is found iteratively. The collision risk is estimated either via the instantaneous probability of collision (IPoC), the maximum instantaneous probability of collision, or the separation distance. This allows for using squared Mahalanobis distance (SMD) to formulate the collision avoidance constraint as an ellipsoidal keep-out zone. The dynamics are automatically linearized via differential algebra, allowing for any dynamical model in the SCP, e.g., high-order gravitational harmonics, atmospheric drag, solar radiation pressure, and third body attraction. The uncertainty of the system is assumed to evolve linearly, so it is propagated using the state transition matrix. Moreover, the station keeping (SK) operational requirement is introduced as a convex constraint, and a sensitivity constraint on the SMD is used to improve the robustness of the maneuver against modeling and actuation errors. A new trust region algorithm based on the nonlinearity index is introduced to avoid artificial unboundedness due to the linearization.

The algorithm is tested on realistic scenarios in GEO and in LEO. The optimizer can recover an optimal solution in all the test cases considered without prior knowledge of the thrust arc structure or thrust direction. It is shown that the computed maneuver can be different when different collision metrics are selected. The algorithm's flexibility allows it to find solutions in high and low-thrust scenarios. The introduction of the novel SMD sensitivity constraint can modify the maneuver significantly, as it constraints the spacecraft on the surface of the keep-out zone where the gradient of SMD is lower. The proposed method is proven reliable and efficient, resulting in a promising step towards autonomous collision avoidance maneuver computation.

Our approach to CAM design is based on the assumption that the state uncertainties are Gaussian during the entire window of interest. Since the propagation windows are relatively short (e.g., one or two orbital periods) and the initial uncertainties are limited this assumption is not a strong one. If we were to consider longer propagation windows or

larger uncertainties, nonlinear uncertainty propagation methods, like Gaussian mixture models (GMMs), should be considered. Alternatively, different representations of the states, like generalized equinoctial elements, can be used to preserve the normality of the distribution.

Funding Sources

This material is based upon work supported by the Air Force Office of Scientific Research under award number FA2386-21-1-4115.

References

- [1] ESOC, “ESA’s Annual Space Environment Report,” Tech. rep., ESA, 2023.
- [2] Letizia, F., Colombo, C., and Lewis, H. G., “Collision Probability Due to Space Debris Clouds Through a Continuum Approach,” *Journal of Guidance, Control, and Dynamics*, Vol. 39, No. 10, 2015, pp. 2240–2249. <https://doi.org/10.2514/1.G001382>.
- [3] Zhang, H., Li, Z., Wang, W., Zhang, Y., and Wang, H., “Geostationary Orbital Debris Collision Hazard after a Collision,” *Aerospace*, Vol. 9, No. 258, 2022. <https://doi.org/10.3390/aerospace9050258>, URL <https://doi.org/10.3390/aerospace9050258>.
- [4] Zhang, Y., Li, B., Liu, H., and Sang, J., “An analysis of close approaches and probability of collisions between LEO resident space objects and mega constellations,” *Geo-spatial Information Science*, Vol. 25, No. 1, 2022, pp. 104–120. <https://doi.org/10.1080/10095020.2022.2031313>.
- [5] Browns, A. C., “Human Spaceflight Recent Conjunctions of Interest Human Spaceflight Screening and Notification,” *Proceedings of the USSTRATCOM Conjunction Summary Message Workshop*, 2010, p. 3.
- [6] Hernando-Ayuso, J., and Bombardelli, C., “Low-thrust collision avoidance in circular orbits,” *Journal of Guidance, Control, and Dynamics*, Vol. 44, No. 5, 2021, pp. 983–995. <https://doi.org/10.2514/1.G005547>.
- [7] Armellin, R., “Collision avoidance maneuver optimization with a multiple-impulse convex formulation,” *Acta Astronautica*, Vol. 186, 2021, pp. 347–362. <https://doi.org/10.1016/j.actaastro.2021.05.046>.
- [8] De Vittori, A., Palermo, M. F., Di Lizia, P., and Armellin, R., “Low-Thrust Collision Avoidance Maneuver Optimization,” *Journal of Guidance, Control, and Dynamics*, Vol. 45, No. 10, 2022, pp. 1815–1829. <https://doi.org/10.2514/1.G006630>.
- [9] Núñez Garzón, U. E., and Lightsey, E. G., “Relating Collision Probability and Separation Indicators in Spacecraft Formation Collision Risk Analysis,” *Journal of Guidance, Control, and Dynamics*, Vol. 45, No. 3, 2022, pp. 517–532. <https://doi.org/10.2514/1.G005744>.
- [10] Patera, R., “Satellite Collision Probability for Non-Linear Relative Motion,” *AIAA/AAS Astrodynamics Specialist Conference and Exhibit*, Vol. 26, American Institute of Aeronautics and Astronautics, Reston, Virginia, 2002. <https://doi.org/10.2514/6.2002-4632>.

- [11] Coppola, V. T., “Including velocity uncertainty in the probability of collision between space objects,” *AIAA/AAS Astrodynamics Specialist Conference 2014*, Vol. 143, San Diego, California, 2012, pp. 2159–2178.
- [12] Alfano, S., “Addressing Nonlinear Relative Motion For Spacecraft Collision Probability,” *AIAA/AAS Astrodynamics Specialist Conference and Exhibit*, American Institute of Aeronautics and Astronautics, Reston, Virginia, 2006, pp. 1–10. <https://doi.org/10.2514/6.2006-6760>.
- [13] Alfano, S., “Eliminating Assumptions Regarding Satellite Conjunction Analysis,” *The Journal of the Astronautical Sciences*, Vol. 59, 2014, pp. 676–705. <https://doi.org/10.1007/s40295-014-0002-4>.
- [14] Xu, X.-l., and Xiong, Y.-q., “A Research on the Collision Probability Calculation of Space Debris for Nonlinear Relative Motions†,” *Chinese Astronomy and Astrophysics*, Vol. 35, No. 3, 2011, pp. 304–317. <https://doi.org/10.1016/j.chinastron.2011.07.008>.
- [15] Wen, C., and Qiao, D., “Calculating collision probability for long-term satellite encounters through the reachable domain method,” *Astrodynamics*, Vol. 6, No. 2, 2022, pp. 141–159. <https://doi.org/10.1007/s42064-021-0119-8>.
- [16] Chan, K., *Spacecraft Collision Probability*, The Aerospace Press, El Segundo, USA, 2008.
- [17] Jones, B. A., and Doostan, A., “Satellite collision probability estimation using polynomial chaos expansions,” *Advances in Space Research*, Vol. 52, No. 11, 2013, pp. 1860–1875. <https://doi.org/10.1016/j.asr.2013.08.027>, URL <http://dx.doi.org/10.1016/j.asr.2013.08.027>.
- [18] Adurthi, N., and Singla, P., “Conjugate unscented transformation-based approach for accurate conjunction analysis,” *Journal of Guidance, Control, and Dynamics*, Vol. 38, No. 9, 2015, pp. 1642–1658. <https://doi.org/10.2514/1.G001027>.
- [19] Zhang, S., Fu, T., Chen, D., and Cao, H., “Satellite instantaneous collision probability computation using equivalent volume cuboids,” *Journal of Guidance, Control, and Dynamics*, Vol. 43, No. 9, 2020, pp. 1757–1763. <https://doi.org/10.2514/1.G004711>.
- [20] Mueller, J., “Onboard Planning of Collision Avoidance Maneuvers Using Robust Optimization,” *AIAA Infotech@Aerospace Conference*, American Institute of Aeronautics and Astronautics, Reston, Virginia, 2009. <https://doi.org/10.2514/6.2009-2051>, URL <https://arc.aiaa.org/doi/10.2514/6.2009-2051>.
- [21] Serra, R., Arzelier, D., Joldes, M., and Rondepierre, A., “Probabilistic Collision Avoidance for Long-term Space Encounters via Risk Selection,” *Advances in Aerospace Guidance, Navigation and Control*, Springer International Publishing, 2015, pp. 679–698. https://doi.org/10.1007/978-3-319-17518-8_39.
- [22] Liu, X., Lu, P., and Pan, B., “Survey of convex optimization for aerospace applications,” *Astrodynamics*, Vol. 1, No. 1, 2017, pp. 23–40. <https://doi.org/10.1007/s42064-017-0003-8>.
- [23] Dutta, S., and Misra, A. K., “Convex optimization of collision avoidance maneuvers in the presence of uncertainty,” *Acta Astronautica*, Vol. 197, 2022, pp. 257–268. <https://doi.org/10.1016/j.actaastro.2022.05.038>.
- [24] Pinson, R., and Lu, P., “Trajectory design employing convex optimization for landing on irregularly shaped asteroids,” *Journal of Guidance, Control, and Dynamics*, Vol. 41, No. 6, 2018, pp. 1243–1256. <https://doi.org/10.2514/1.G003045>.

- [25] Alonso-Mora, J., Montijano, E., Nägeli, T., Hilliges, O., Schwager, M., and Rus, D., “Distributed multi-robot formation control in dynamic environments,” *Autonomous Robots*, Vol. 43, No. 5, 2019, pp. 1079–1100. <https://doi.org/10.1007/s10514-018-9783-9>.
- [26] Pirovano, L., and Armellin, R., “Detection and estimation of spacecraft maneuvers for catalog maintenance,” *Acta Astronautica*, Vol. 215, No. December 2023, 2024, pp. 387–397. <https://doi.org/10.1016/j.actaastro.2023.12.016>.
- [27] Boyd, S., and Vandenberghe, L., *Convex Optimization*, Cambridge University Press, Cambridge, NY, 2004.
- [28] Lew, T., Bonalli, R., and Pavone, M., “Chance-Constrained Sequential Convex Programming for Robust Trajectory Optimization,” *2020 European Control Conference (ECC)*, IEEE, 2020, pp. 1871–1878. <https://doi.org/10.23919/ECC51009.2020.9143595>.
- [29] Ridderhof, J., Pilipovsky, J., and Tsiotras, P., “Chance-Constrained Covariance Control for Low-Thrust Minimum-Fuel Trajectory Optimization,” *2020 AAS/AIAA Astrodynamics Specialist Conference*, South Lake Tahoe, CA, 2020, pp. 9–13.
- [30] Benedikter, B., Zavoli, A., Wang, Z., Pizzurro, S., and Cavallini, E., “Covariance Control for Stochastic Low-Thrust Trajectory Optimization,” *AIAA SciTech 2022 Forum*, American Institute of Aeronautics and Astronautics, Reston, Virginia, 2022. <https://doi.org/10.2514/6.2022-2474>.
- [31] Benedikter, B., Zavoli, A., Wang, Z., Pizzurro, S., and Cavallini, E., “Convex Approach to Covariance Control with Application to Stochastic Low-Thrust Trajectory Optimization,” *Journal of Guidance, Control, and Dynamics*, Vol. 45, No. 11, 2022, pp. 2061–2075. <https://doi.org/10.2514/1.G006806>.
- [32] Mueller, J. B., Griesemer, P. R., and Thomas, S. J., “Avoidance maneuver planning incorporating station-keeping constraints and automatic relaxation,” *Journal of Aerospace Information Systems*, Vol. 10, No. 6, 2013, pp. 306–322. <https://doi.org/10.2514/1.54971>.
- [33] Malyuta, D., Reynolds, T. P., Szmuk, M., Lew, T., Bonalli, R., Pavone, M., and Açıkmeşe, B., “Convex Optimization for Trajectory Generation: A Tutorial on Generating Dynamically Feasible Trajectories Reliably and Efficiently,” *IEEE Control Systems*, Vol. 42, No. 5, 2022, pp. 40–113. <https://doi.org/10.1109/MCS.2022.3187542>, URL <https://ieeexplore.ieee.org/document/9905530/>.
- [34] Losacco, M., Fossà, A., and Armellin, R., “Low-Order Automatic Domain Splitting Approach for Nonlinear Uncertainty Mapping,” *Journal of Guidance, Control, and Dynamics*, 2024, pp. 1–20. <https://doi.org/10.2514/1.G007271>.
- [35] Bernardini, N., Wijayatunga, M. C., Baresi, N., and Armellin, R., “State-Dependent Trust Region for Successive Convex Optimization of Spacecraft Trajectories,” *AAS/AIAA Space Flight Mechanics Meeting*, Austin, TX, 2023, pp. 1–20.
- [36] Morselli, A., Armellin, R., Di Lizia, P., and Bernelli Zazzera, F., “A high order method for orbital conjunctions analysis: Sensitivity to initial uncertainties,” *Advances in Space Research*, Vol. 53, No. 3, 2014, pp. 490–508. <https://doi.org/10.1016/j.asr.2013.11.038>.
- [37] Baù, G., Hernando-Ayuso, J., and Bombardelli, C., “A generalization of the equinoctial orbital elements,” *Celestial Mechanics and Dynamical Astronomy*, Vol. 133, No. 11-12, 2021. <https://doi.org/10.1007/s10569-021-10049-1>.

- [38] Vittaldev, V., and Russell, R. P., “Space object collision probability using multidirectional Gaussian mixture models,” *Journal of Guidance, Control, and Dynamics*, Vol. 39, No. 9, 2016, pp. 2161–2167. <https://doi.org/10.2514/1.G001610>.
- [39] Armellin, R., Di Lizia, P., Bernelli-Zazzera, F., and Berz, M., “Asteroid close encounters characterization using differential algebra: The case of Apophis,” *Celestial Mechanics and Dynamical Astronomy*, Vol. 107, No. 4, 2010, pp. 451–470. <https://doi.org/10.1007/s10569-010-9283-5>.
- [40] Alfriend, K. T., Akella, M. R., Frisbee, J., Foster, J. L., Lee, D.-J., and Wilkins, M., “Probability of collision error analysis,” *Space Debris*, 1999. <https://doi.org/https://doi.org/10.1023/A:1010056509803>.
- [41] Alfano, S., “Satellite conjunction Monte Carlo analysis,” *19th AAS/AIAA Space Flight Mechanics Meeting*, Vol. 134, American Astronautical Society, Savannah, Georgia, 2009, pp. 2007–2024.
- [42] Wang, Z., and Grant, M. J., “Minimum-Fuel Low-Thrust Transfers for Spacecraft: A Convex Approach,” *IEEE Transactions on Aerospace and Electronic Systems*, Vol. 54, No. 5, 2018, pp. 2274–2290. <https://doi.org/10.1109/TAES.2018.2812558>.
- [43] Mao, Y., and Acikmese, B., “SCvx-fast: A Superlinearly Convergent Algorithm for A Class of Non-Convex Optimal Control Problems,” *ArXiv*, Vol. 2112, 2021. URL <http://arxiv.org/abs/2112.00108>.
- [44] Bombardelli, C., and Hernando-Ayuso, J., “Optimal impulsive collision avoidance in low earth orbit,” *Journal of Guidance, Control, and Dynamics*, Vol. 38, AIAA International, 2015, pp. 217–225. <https://doi.org/10.2514/1.G000742>.
- [45] Pavanello, Z., Pirovano, L., and Armellin, R., “Long-Term Encounters Collision Avoidance Maneuver Optimization with a Convex Formulation,” *AAS/AIAA Space Flight Mechanics Meeting*, Austin, TX, 2023, pp. 1–20.

A. High level flow of the SCP

In Appendix A the algorithm of the SCP is shown.

```

1: Get inputs for the spacecraft:  $HBR, A_{drag}, C_D, A_{SRP}, C_r, \mathbf{x}_0, \mathbf{C}_0$ 
2: Assign  $t_0, \Delta t, N, u_{max}, u_{min}, \bar{P}_{IC}$  (or  $\bar{P}_{IC,m}$  or  $\bar{d}_{miss}$ ),  $\rho, \varepsilon, \bar{v}, \text{tol}_M, \text{tol}_m, j_{max}, k_{max}$ 
3:  $t \leftarrow t_0 : \Delta t : t_0 + N\Delta t$ 
4: Perform a first-order DA propagation of the secondary trajectory starting from  $\mathbf{x}_{s,0}$ .
5: for  $i = 1 : N$  do
6:    $\bar{\mathbf{x}}_{s,i} \leftarrow$  constant part of the propagation
7:    $A_{s,i} \leftarrow$  linear part of the propagation
8:    $C_{s,i} \leftarrow$  Eq. (24b)
9:    $P_{s,i} \leftarrow$  Eq. (25b)
10: end for
11:  $j \leftarrow 0$ 
12: while  $\|\mathbb{w}^j - \mathbb{w}^{j-1}\|_\infty > \text{tol}_M \wedge j < j_{max}$  do
13:    $j \leftarrow j + 1$ 
14:    $k \leftarrow 0$ 
15:   if  $j > 1$  then
16:     Perform a second-order DA propagation with control history  $\mathbb{w}^{j-1}$  and expansion points from  $\mathbb{x}^{j-1}$ .
17:   else
18:     Perform a second-order forward DA propagation with no control.
19:   end if
20:   for  $i = 0 : N$  do
21:      $\bar{\mathbf{x}}_i^j, \bar{\boldsymbol{\phi}}_i^j \leftarrow$  constant part of the propagation geodetic coordinates
22:      $A_i^j, B_i^j, G_i^j \leftarrow$  linear part of the propagation and geodetic coordinates transformation
23:      $C_{p,i}^j \leftarrow$  Eq. (24a)
24:      $P_{p,i}^j \leftarrow$  Eq. (25a)
25:      $P_i^j \leftarrow$  Eq. (26)
26:      $\mathbf{r}_i^j \leftarrow \mathbf{r}_{p,i}^j - \mathbf{r}_{s,i}$ 
27:      $(\bar{d}_m^2)_i^j \leftarrow$  Eq. (15a), Eq. (15b), or Problem (17)
28:      $(d_m^2)_i^j \leftarrow$  Eq. (11)
29:      $(P_{IC})_i^j \leftarrow$  Eq. (13)
30:      $\xi_i \leftarrow$  Eq. (57)
31:     if  $(P_{IC,i}^j > (1 - \varepsilon)\bar{P}_{IC})$  then
32:        $\gamma_i \leftarrow$  Eq. (41)
33:     end if
34:   end for
35:   for  $i = 1 : N \wedge (d_m^2)_i^j < (\bar{d}_m^2)_i^j$  do
36:     Find starting point on the ellipsoid's surface using Eq. (33)
37:   end for
38:   while  $(\|\mathbf{r}^{j,k} - \mathbf{r}^{j,k-1}\|_\infty > \text{tol}_m \wedge k < k_{max})$  do
39:      $k \leftarrow k + 1$ 
40:     Solve SOCP Problem (63)
41:   end while
42:    $\mathbb{x}^j \leftarrow \mathbb{x}^{j,k}$ 
43:    $\mathbb{w}^j \leftarrow \mathbb{w}^{j,k}$ 
44: end while
45: Validation: Propagate forward from the initial state using the control history from the last iteration and check the highest position error with respect to the last major iteration.

```
